Geochemistry and Petrology of the Tia Maria Prospect, Department of Arequipa, Peru

By
Andrew P. Mioduchowski

Submitted in Partial Fulfillment of the Requirements for the
Degree of Master of Science in Geology

Department of Earth and Environmental Sciences
New Mexico Institute of Mining and Technology
Socorro, NM 87801
February 2001

Abstract

Tia Maria is a copper prospect is located in Arequipa department of Peru. Petrographic, fluid inclusion and stable isotopic analyses were carried out on samples taken from drill core and outcrop in the pursuit of three objectives: 1) Description of the supergene oxide mineralization and deduction of the hypogene mineralization and the conditions of its oxidation; 2) characterization of the mineralizing fluids and by inference their source; and 3) examination of the relationship between the Tia Maria Cu mineralization and the adjacent Rosa Maria Cu-Au mineralization and the presentation of an overall genetic model.

Tia Maria is a porphyry system that is thought to be 145 to 160 Ma in age (Clark 1990a) and occurs in the Fiscal Pluton, a part of the Peruvian Coastal Batholith, and in surrounding rocks of the Precambrian Arequipa Massif. Mineralization is in the form of a single generation of narrow (< 4 cm wide) quartz-chalcopyrite-pyrite stockwork veins. No sheeted dykes or mineralized breccias have been observed. The crosscutting, Au-bearing Rosa Maria quartz-pyrite-specularite-chalcopyrite veins are vuggy, have multiple generations and are up to several meters wide. The granitic host rocks show a pattern of patchy K-silicate stable (biotite) alteration, overprinted by propylitic (chlorite $\pm$ rutile $\pm$ epidote $\pm$ magnetite) alteration and sericite (sericite $\pm$ quartz). There is no argillic alteration cap.

The prospect is oxidized to a depth of up to 300 m although there is no leached cap or enrichment blanket. The copper oxide mineralization, dominantly chrysocolla and malachite, is concentrated in joints and fractures in the host rocks. This is felt to be the product of neutral pH, *in-situ* oxidation of a chalcopyrite dominated (CuS_x : FeS_x > 5:1) protore.

Fluid inclusions from the Tia Maria veins are dominantly two phase, liquid dominated (F > 0.80), with no daughter minerals or evidence of CO_2 and average less then 8 mm in size. There is no evidence of boiling. Homogenization temperatures ranged from 323 to 397 °C and averaged 360 °C. Salinity ranged from 3.6 to 13.1 eq. wt. % NaCl and averaged 7.7 eq. wt. % NaCl. Due to the small size of the inclusions (< 1mm), only a few homogenization temperatures were obtained from the Rosa Maria veins, ranging from 250 to 280 °C. There is no T_h versus salinity trend. Calculations using the fluid inclusion data produced steep isochores, indicating a low pressure dependence and a minimum trapping pressure of 200 to 300 bars. Such medium salinity, low to moderate homogenization temperature inclusions that show little or no evidence of boiling are often found in the propylitic zone of porphyry copper deposits. Using the H_2O-NaCl system phase diagrams of Bowers and Helgeson (1983), an upper pressure-temperature range of ~ 350 bar and 425 °C was constrained.

Oxygen isotopic analysis was carried out on Tia Maria and Rosa Maria vein quartz and on altered and relatively unaltered host rocks. The Tia Maria quartz veins averaged 9.0 $^{o}/_{oo}$, with a range of 0.9 $^{o}/_{oo}$. The Rosa Maria veins averaged 12.3 $^{o}/_{oo}$, with a range of 4.9 $^{o}/_{oo}$. Whole rock samples taken from the mineralized area had a $d^{18}O$ range of 8.5 to 9.5 $^{o}/_{oo}$ (independent of the degree of alteration) while distal samples averaged ~ 11 $^{o}/_{oo}$. Using a temperature of 360 ^{o}C a quartz-water fractionation of ~ 5 $^{o}/_{oo}$ was calculated, resulting in an average mineralizing fluid value of ~ 4 $^{o}/_{oo}$. Recalculating using the upper limit temperature of 425 ^{o}C, the result was ~ 5.4 $^{o}/_{oo}$. In either case, it can be stated that the mineralizing fluids were dominantly of magmatic origin. The relatively small isotopic shift of the host rocks combined with the generally muted alteration regime, suggests that this system had a low water to rock ratio.

The lack of water, the single episode of mineralization and an alteration pattern that suggests a location that is farther from the intrusive but below the upper levels of the system points to derivation from a deep intrusive. Due to the higher solubility of water in deeper intrusives, only limited quantities of volatiles are exsolved from such systems.

The textural differences, lower temperatures and evidence of boiling suggest that the Rosa Maria veins formed in a lower pressure regime than did Tia Maria. Rosa Maria may be an epithermal type system that formed as the Tia Maria porphyry system was collapsing and pressure dropped from lithostatic to hydrostatic.

Acknowledgements

I would like to acknowledge the people without whom my graduate studies would not have been possible. Special thanks go to my advisor, Dr. Andy Campbell, for his support, patience, knowledge and constructive criticism. I am grateful to Dr. William X. Chavez for arraigning this research and for his valuable insights into copper systems. I would also like to thank my third committee member, Dr. David I. Norman, for his assistance and thoughtful review.

I would like to thank Rio Tinto Peru, especially Dave Andrews and Nick Hawks, for providing and funding this project as well as the Earth and Environmental Sciences Department at the New Mexico Institute of Mining and Technology for funding my graduate studies.

Finally, thanks go to my friends and fellow students here at Tech, especially Chadwick J. Spencer, for their moral support and for making graduate school an enjoyable experience.

Table of Contents

List of Tables

List of Figures

List of Appendices

Introduction

Porphyry-type deposits of the Andean region of South America are the source of a major proportion of the world's copper production. Although there is some debate over the exact definition of what exactly constitutes a copper porphyry, it is generally accepted to have low to medium grade, large tonnage, chalcopyrite/pyrite/molybdenite mineralization with potassic-propylitic metasomatic and phyllic hydrolitic alteration related to upper mantle derived calc-alkaline intrusives (Guilbert and Park, 1986; Williams and Forrester, 1995). Due to a long period of sustained low commodities prices, supergene enriched mineralization has gained in importance in the economic evaluation of porphyry copper systems as the extraction of copper from supergene "copper oxide" minerals (actually an assemblage of oxides, carbonates, phosphates, sulfates, silicates, secondary sulfides etc.) by leaching is significantly easier and cheaper then by concentration and smelting from the generally lower grade hypogene sulfides.

Southwestern Peru contains a variety of ore deposits, including skarns, copper-gold, hematite, and polymetallic epithermal-type veins and the Cerro Verde, Cuajone, Toquepala and Quellaveco copper porphyries. The region is being actively explored. The Tia Maria prospect is in the southwest of Arequipa department, along the Pacific coast some 30 km west of the boundary with Moquegua department (Fig. 1).

The now abandoned Rosa Maria workings, listed incorrectly as a silver district in the Atlas of Mining and Energy in Peru (Benavides and Espinoza, 1998) exploited the scattered, gold bearing, quartz-pyrite-specularite-chalcopyrite veins in the area (Fig. 2) (Bellido and Guevara, 1961; Clark et al., 1990a). Although Clark et al. (1990a) implied that the quartz-chalcopyrite-pyrite stockwork veins that comprise the Tia Maria prospect were either related to, or similar to, the Rosa Maria veins, initial exploration

Figure. 1. General geographic location of the Tia Maria Prospect. Modified after Expedia.com Travel website.

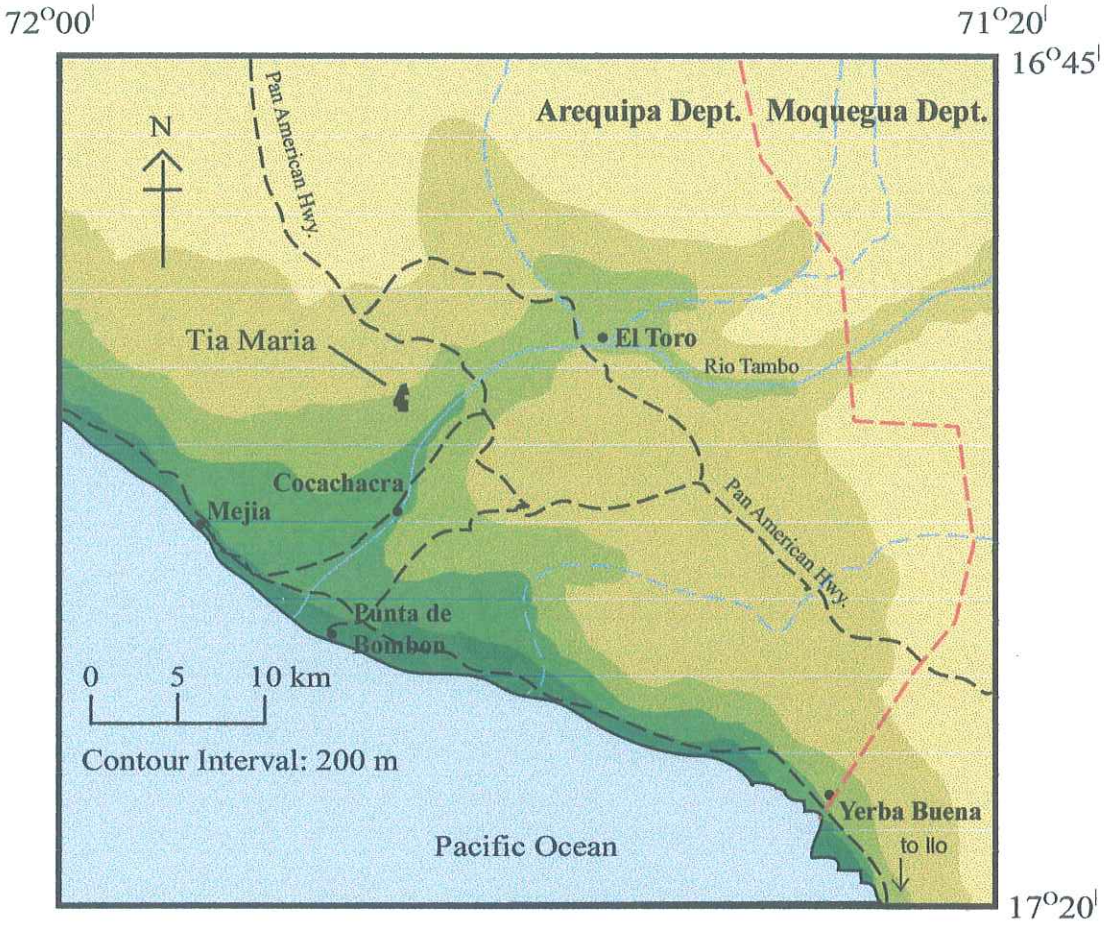
72°00'
71°20'
16°45'
17°20'
N
Pan American Hwy.
Arequipa Dept.
Moquegua Dept.
Tia Maria
El Toro
Rio Tambo
Cocachacra
Mejia
Pan American Hwy.
Punta de Bombon
0 5 10 km
Contour Interval: 200 m
Yerba Buena
to Ilo
Pacific Ocean


PERU
LIMA
Toquepala
Quellaveco
Cuajone
0 100 200 km
Cerro Verde
Tia Maria

Figure. 2. Geology of the Tia Maria area. Modified after Bellido and Guevara (1961), Garcia and Landa (1968) and Cobbing et al. (1984). Formation names are those of the original Peruvian mapsheet. Note the much wider distribution of the Rosa Maria-type veins relative to that of the Tia Maria mineralization.

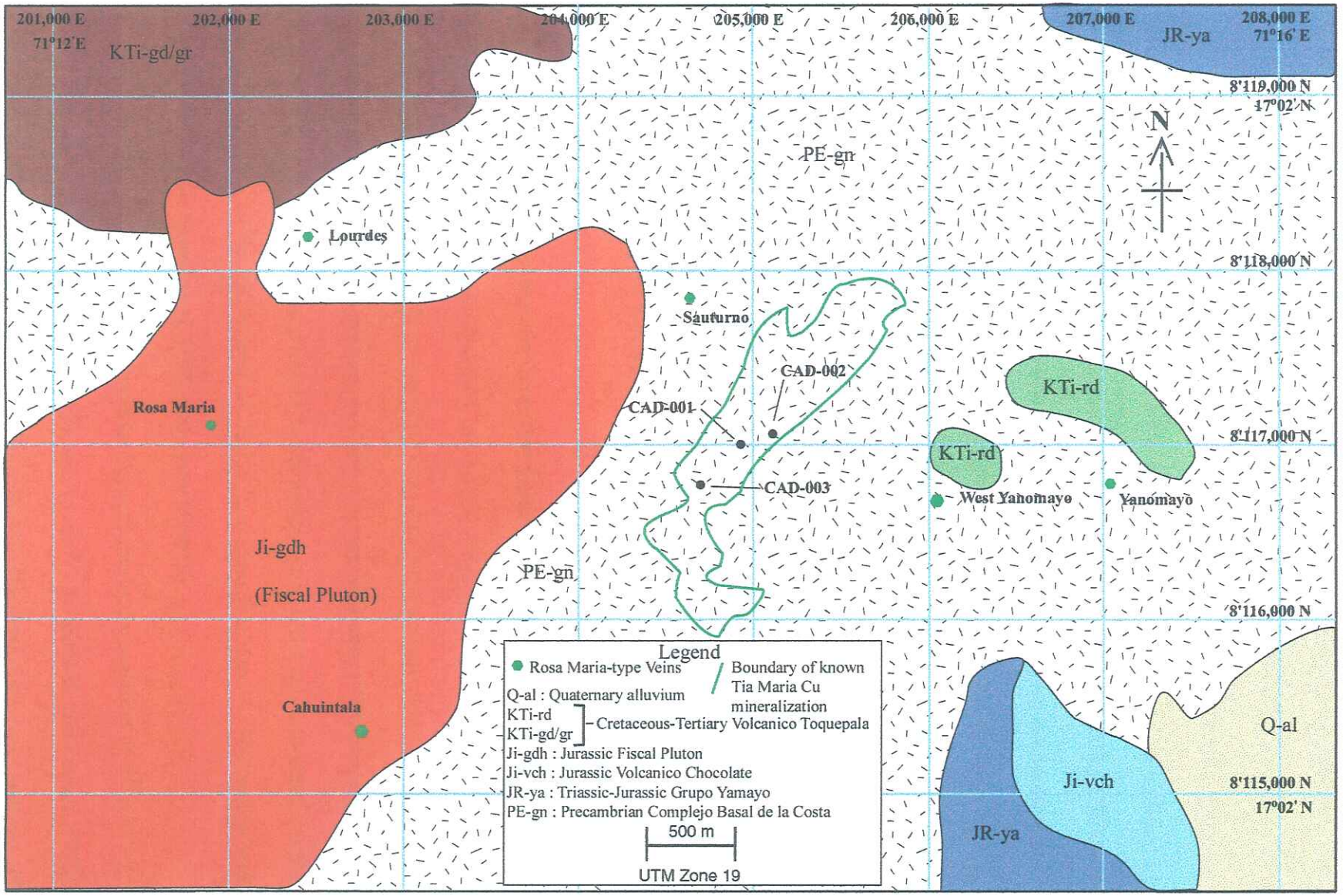
201,000 E
71°12'E
202,000 E
203,000 E
204,000 E
205,000 E
206,000 E
207,000 E
208,000 E
71°16' E
KTi-gd/gr
JR-ya
8'119,000 N
17°02' N
N
PE-gn
Lourdes
8'118,000 N
Sauturno
CAD-002
CAD-001
KTi-rd
Rosa Maria
8'117,000 N
KTi-rd
CAD-003
West Yanomayo
Yanomayo
Ji-gdh
(Fiscal Pluton)
PE-gn
8'116,000 N
Legend
Rosa Maria-type Veins
Boundary of known Tia Maria Cu mineralization
Q-al : Quaternary alluvium
KTi-rd
KTi-gd/gr
Cretaceous-Tertiary Volcanico Toquepala
Ji-gdh : Jurassic Fiscal Pluton
Ji-vch : Jurassic Volcanico Chocolate
JR-ya : Triassic-Jurassic Grupo Yamayo
PE-gn : Precambrian Complejo Basal de la Costa
500 m
UTM Zone 19
Cahuintala
Q-al
Ji-vch
8'115,000 N
17°02' N
JR-ya

work has revealed textural and mineralogical differences that suggest a porphyry style of mineralization (Dave Andrews, Rio Tinto Peru, pers. com., 1999).

Inferring hypogene mineralogy and the conditions under which protores are oxidized using supergene mineralogy is a well-established technique, as exemplified by Locke (1926), Sato (1960) and Anderson (1982) and recently summarized by Chavez (2000). The mineralogy of the oxide zone and its mode of occurrence is important in determining whether copper can be efficiently and economically removed from ore. Efficient leaching depends on the ability of the leaching solution to flow freely, and to have a large surface area of contact with copper minerals. Both these criteria are greatly enhanced if the oxides occur on fractures, as this is where the rock will naturally break during crushing. Certain elements, such as manganese and chlorine for example, that can occur with copper oxides, negatively effect copper recovery by complicating metallurgy when the copper is removed from the leach solutions (Murr, 1980; Biswas and Davenport, 1994).

It is well accepted that the fluids that form a porphyry-style Cu deposit are sulfur-rich magmatic volatiles that have condensed while flowing upwards and mixed with meteoric fluids derived from marginally located, convectively circulating, meteoric cells that move inward as the system cools (Henley and McNabb, 1978; Eastoe, 1982; Sillitoe 1989). A point of disagreement is the relative proportion and importance of the meteoric fluids, a factor which certainly varies from deposit to deposit (Hedenquist and Lowenstern, 1994; Sheets et al, 1996; and many others).

Magmatic waters generally have an oxygen isotope composition of $\delta^{18}O$ of ~ 5 to 10 $^{o}/_{oo}$ and most meteoric waters ~ 0 (ocean) to -25 $^{o}/_{oo}$ (Campbell and Larson, 1998), so inferences about the sources of the mineralizing fluids can be made from analyses of

mineralizing veins and altered wallrocks. As most porphyry fluids have $d^{18}O$ values that fall between that of traditional magmatic water and the meteoric water line (Hedenquist and Lowenstern, 1994), it might be thought that the fluid mixing path is a simple one. There are complications, however. Deeply circulating meteoric waters tend to become substantially enriched in ^{18}O and may have only a small impact on the $d^{18}O$ of magma derived fluids (Nesbitt and Muehlenbachs, 1995). Stable isotope halos in altered wallrocks depend greatly on the water/rock ratios (w/r), as a w/r of less than 1 will result in little or no shift in the isotopic value of the wallrock while the isotopic value of the mineralizing fluid will shift towards that of the wallrock (Field and Fifarek, 1985). Furthermore, in the case of Tia Maria, the surface waters that would have affected its formation may have been derived from ocean waters (see below for geologic setting), which has a $d^{18}O$ of 0 $^{o}/_{oo}$, making any isotopic shift even smaller. Seawater is thought to have had a more or less constant $d^{18}O$ over time, with possibly a slight decrease detected in older samples (Hoefs, 1997).

The first objective of the study was to characterize the supergene oxide mineralization present at Tia Maria, and based on this, make deductions about the hypogene mineralogy and the geochemical conditions of oxidation. This was accomplished by taking a representative sample of oxides from outcrop and drill core and analyzing them by electron microprobe and x-ray diffraction. This included analyzing minerals such as hematite for accessory copper content.

The second objective of this study was to characterize the mineralizing fluids and to infer their source. This was accomplished by investigating the fluid inclusions in the quartz veins at Tia Maria and the oxygen isotope signatures of the quartz veins as

well as that of the altered and unaltered host rocks. A petrographic study, using optical microscopy, was also carried out.

The final objective of this study was to use the evidence collected in the course of fulfilling the first two objectives to determine the relationship between the Rosa Maria and Tia Maria mineralization and to present a genetic model.

Regional Geology

Southwestern Peru is largely underlain by granulite to amphibolite grade gneisses of the Arequipa Massif. It is thought that the Arequipa Massif, along with other fragments of crystalline basement, may be the reworked remains of the ancient margin of Gondwanaland. Geochronological studies on the Arequippa Massif have resulted in an age range of 2000 to 600 Ma (Shackleton et al., 1979; Cobbing, 1985) and the older end of the range may represent a distal expression of the Trans-Amazonian event of the Brazilian Shield (Cobbing, 1985). This was overlain in the Paleozoic by a variety of sedimentary strata.

During the Mesozoic era, fault-controlled troughs that opened in response to ensialic spreading (confined to the sialic, or silica and aluminum rich upper levels of the Earth's crust) were established on the Pacific margin of the South American craton. The western most of these troughs is the Huarmey-Canete basin, which represents a marginal basin that failed to develop into an oceanic rift. During this period, the basin filled with arc volcanics, volcaniclastics and sediments derived from repeated marine transgressions. These sediments and volcanics also occur farther south, in the southern Arequipa segment and the Toquepala segment and outcrop to the east and southeast of Tia Maria. A compressional event closed up the extensional basin at about 100 Ma and this was followed by a number of compressional and extensional episodes, linked to

changes in the convergence rate between the continental and oceanic plates, throughout the Cretaceous and Paleogene (Pitcher, 1984; Jaillard and Soler, 1996).

Gravity surveys indicate that this marginal basin is underlain by a huge arch structure that extends from Trujillo in the north to Arequipa in the south. This is a wedge of material that at 3.0 g/cm^3 is much denser then the 2.75 g/cm^3 Arequipa massif and could either be imbricate oceanic crust or an intrusion of upper mantle material. Further south, the crust is of density similar to that of the Arequipa Massif for most of its thickness. This change could be the result of either a more steeply dipping subduction zone where the oceanic slab has smoothly passed below the continental plate or, alternately, could be the result of tectonic underplating of the crust by subducted sediments (Atherton, 1984; Pitcher, 1984; Megard, 1987).

The Coastal Batholith of Peru is a complex of over 1000 plutons that stretches from Piura in the north, near the border with Ecuador, to Toquepala, near the Chilean border, in the south (Fig. 3). While this zone has a length almost 2000 km, its width rarely exceeds 65 km. The batholith is divided into five parts from north to south: the Piura, Trujillo, Lima, Arequipa and Toquepala segments. The Lima segment, the southern half of the Trujillo segment and the northern half of the Arequipa segment, which combined represent over 80% of the Coastal Batholith, intrude the Huarmey-Canete marginal basin. In the north, the Piura segment and the northern half of the Trujillo segment intrude a Precambrian to Paleozoic schist belt. In the south, the southern half of the Arequipa segment and the Toquepala segment intrude the Arequipa Massif (Atherton, 1984; Pitcher, 1984).

The emplacement of the Coastal Batholith spans a large portion of the Mesozoic and Cenozoic. While the majority was emplaced between 100 and 60 Ma, the Punta

Figure 3. The Coastal Batholith of Peru. Note its extreme length relative to its width. Tia Maria is a part of the Toquepala segment, as are Cerro Verde and the Toquepala area porphyries. After Atherton (1984).

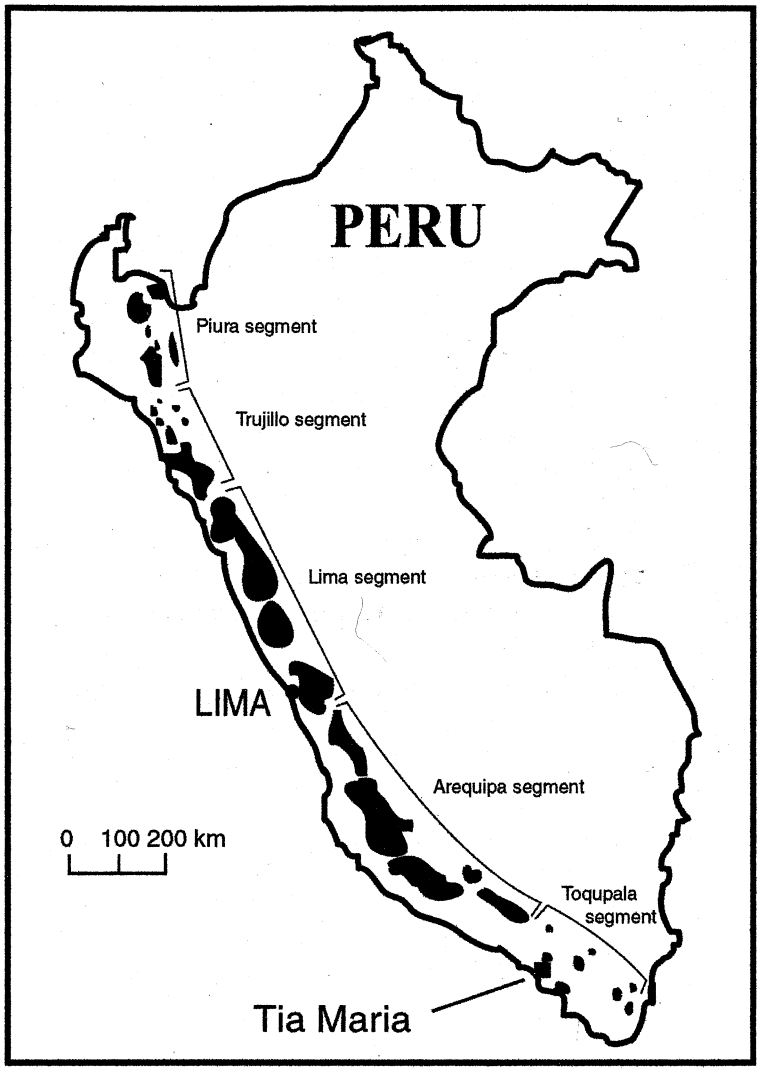
PERU
Piura segment
Trujillo segment
Lima segment
LIMA
Arequipa segment
0 100 200 km
Toqupala segment
Tia Maria

Coles suite of the Toquepala segment is as old as190 Ma. Although the Patavilca suite is assigned to the Lima segment, the fact that it intruded as late as 34 Ma, some 25 Ma after the next most recent intrusive event, suggests that it may represent a separate pulse of igneous activity. (Aguirre et al., 1984; Cobbing and Moore, 1984; Vidal, 1985).

Mineralization is not distributed evenly through the Coastal Batholith. Most mineral deposits are found in the central to southern portion of the Arequipa segment and scattered throughout the Toquepala segment. Despite a similar level of erosion, the Lima and Trujillo segments are relatively barren.

Volcanogenic, layered barite-base metal sulfide deposits and strata-bound amphibole-magnetite-chalcopyrite deposits are associated with mid to late Cretaceous volcanic host rocks. Pluton-related deposits include mid-Cretaceous, gabbro associated, amphibole-magnetite-chalcopyrite veins and late Cretaceous, granite associated quartz-specularite-chalcopyrite veins, chalcopyrite-molybdenite-scheelite skarns, quartz-calcite-auriferous pyrite veins and porphyry type chalcopyrite-molybdenite-pyrite disseminations and stockworks. The Arequipa segment contains a cluster of mid-late Cretaceous porphyry-type mineralization in the Rio Pisco area (Agar, 1981). The Toquepala segment hosts the Cerro Verde, Toquepala, Cuajone and Quellaveco copper porphyries, which are of late Paleocene age (Vidal, 1985).

Quartz-specularite-chalcopyrite type veins, mineralogically similar to the Rosa Maria veins, have been exploited to the southwest, near Ilo. This type of vein in fact occurs up and down the coast in the Toquepala segment, though only rarely is it of economic value (Chavez, 2000).

Atherton (1984) considers the Coastal Batholith of Peru to be particularly suited to demonstrate the effects (or the lack there of) of crustal contamination on mantle

derived melts for, as noted above, the Coastal Batholith intrudes a wide variety of host rocks. Individual segments, such as the Arequipa segment, pass from one type of host rock to another with only a very limited change in their characteristics. This petrographic observation is well substantiated by trace element and isotopic analysis.

Atherton et al. (1979) present a number of $^{87}Sr/^{86}Sr$ values from related plutons in the Lima segment that average ~ 0.704 and do not show a shift over their ~15 Ma age range. They feel that this may represent the high-level differentiation of mantle derived material with little crustal component.

Barreiro (1984) presents $^{206}Pb/^{204}Pb$ data comparing the southern Peru basement gneisses, with a $^{206}Pb/^{204}Pb$ ratio of ~ 16.0 to 17.0, to the Jurassic to Eocene plutonic rocks from near Toquepala, with a $^{206}Pb/^{204}Pb$ ratio of ~ 18.6. Most MORB and ocean-island volcanics fall between 18.0 and 19.0. Some late Cenozoic volcanics from southern Peru fall at about 17.0, indicating some crustal assimilation.

Musaka and Tilton (1984) present more geographically constrained lead isotope data. Samples from the Arequipa segment have a $^{206}Pb/^{204}Pb$ value of ~ 18.4 while samples from the Lima segment have values of ~ 18.8. Based on $^{207}Pb/^{204}Pb$ data that is significantly higher then the Ocean Regression Line, they feel that magma reservoir represents homogeneous, enriched sub-continental mantle. As with Barreiro (1984), they feel that although there has been some limited crustal assimilation, especially in the Arequipa segment, the batholith evolved mainly through fractional crystallization.

Atherton and Sanderson (1985) and Boily et al. (1989) both present a large quantity of REE, trace element and stable isotopic data that supports an origin based on the successive evolution of partially crystallized melts. Atherton and Sanderson (1985) feel that Coastal Batholith derives from the partial melting enriched spinel peridotites

with melts being channeled by a major, long lived, structural lineament, related to the extensional basin but continuing beyond it, that tapped the mantle. Therefore, they feel that the Batholith may not, in fact, have been directly related to subduction, although the mantle enrichment was most likely the result of it.

Boily et al. (1989), in a study of the Arequipa and Toquepala segments to the south east of the city of Arequipa, documented a decrease in $\epsilon_{Nd}i$, an increase in $\epsilon_{Sr}i$ and a substantial lowering of the $^{206}Pb/^{204}Pb$ ratio that correlated to the density of Precambrian outcrop. The Ilo suite, which contains Tia Maria, was found to have lower amounts of crustal assimilation then the groups that contain the Cerro Verde porphyry near Arequipa and the porphyries in the Toquepala area. Boily et al (1989) feel that this overall small amount of crustal assimilation could be explained by a stretching and thinning of the Precambrian crust during the Mesozoic extensional regime that caused basin formation farther north. The variation between the plutons could be due to varying amounts of this thinning.

Geology of the Tia Maria Prospect

The Tia Maria prospect is located to the north of the town of Cocachacra, which lies in the valley of the Rio Tambo on the Pacific coast of Arequipa department (Fig. 1).

Mineralization, centered on the Cachuyo Zone outlined in Figure 2, is in the form of quartz-chalcopyrite-pyrite stockwork veins. These crosscut earlier biotite and iron sulfide (now oxidized; see below) veinlets. The quartz-sulfide stockwork is of a single generation and individual veins rarely exceed 4 cm in width. The fracture density is relatively low. No sheeted dykes or mineralized breccias have been observed.

In contrast to the Tia Maria veins, the later, crosscutting, gold bearing, quartz-pyrite-specularite-chalcopyrite Rosa Maria veins are large (up to several meters wide)

and are much more broadly distributed (Fig. 2). These veins are vuggy, have euhedral quartz crystals and multiple crosscutting generations. (Clark et al., 1990a; Dave Andrews, Rio Tinto Peru, pers. com., 1999).

The alteration (K silicate-propylitic-sericite) of the granitic host rocks (see below) is generally subdued. Although the prospect is at the surface, the Tia Maria mineralization is visible only to a limited extent in outcrop and alteration is almost invisible. There is no heavy phyllic/argillic altered cap. However, both the mineralization and alteration become evident in even shallow road cuts.

As is typical with sulfide mineralization exposed at the surface in an arid environment (eg., Titley and Marozas, 1995; Chavez, 2000) the prospect has been deeply oxidized, averaging a ~200 m depth below the current surface but down to ~300 m in some areas. The supergene oxides are found throughout the oxidized zone in fractures and joints in the rock. While there are between two and four oxidation paleohorizons, there is no hematite/goethite leached cap or enrichment blanket associated with the Tia Maria mineralization. However, there is abundant supergene hematite in the vicinity of outcropping Rosa Maria veins.

The prospect is emplaced in the Complejo Basal de la Costa, a part of the Arequipa Massif and, in the subsurface, the granitic Fiscal Pluton (Fig. 2). Cobbing and Moore (1984) list the Fiscal Pluton as being a part of the 103 Ma Ilo suite of the Toquepala segment. Clark et al. (1990a), however, reports $^{40}Ar/^{39}Ar$ dates of ~160 Ma for the intrusive and a date of ~145 Ma for crosscutting monzonite dyke that also crosscuts both the Rosa Maria and Tia Maria mineralization. A Jurassic age of mineralization would put Tia Maria among the middle-aged Cu-porphyries in the Andes. Some of the oldest porphyries are in Argentina, ranging in age from ~267 to

281 Ma (Sillitoe, 1977). The porphyries of the Central and Eastern Cordillera of Columbia range from ~140 to 200 Ma (Sillitoe et al. 1982) and the newly reported porphyries in southeastern Ecuador, while not yet radiometrically dated, are thought to be Jurassic in age (Gendall et al., 2000). However, the majority of deposits are younger: The porphyries of northern Chile, including the giant Chuquicamata and Escondida deposits, range in age from ~31 to 42 Ma (Richards et al., 1999). Toquepala, Cerro Verde and the other porphyries of southern Peru range in age from ~52 to 60 Ma (Clark et al., 1990a; Phelps Dodge, 2000). The porphyries of the western Cordillera of Columbia have ages of ~42 to 54 Ma and those of the Cauca-Patia depression (between the Western and Central Cordillera of Columbia) are between ~6 and 17 Ma (Sillitoe et al. 1982). Most of the remainder of the Argentinean deposits range in age from ~7 to 16 Ma (Sillitoe, 1977).

Porphyry deposits tend to occur in spatially and temporally clustered groups, but occasionally a much older deposit is found within such a group. For example, while most of the fifty plus porphyries that are found in Arizona, New Mexico and Sonora (Mexico), have ages of ~52 to 65 Ma, with a few as old as 71 to 74 Ma, the age of the Bisbee deposit, in the southeast corner of Arizona, is ~180 Ma (Keith and Swan, 1995). A similar situation occurs in western Mexico, where most porphyry deposits are related to Laramide magmatism with a sparse distribution of Jurassic and Cretaceous age systems, likely the result of the erosion of the older and shallower deposits (Barton et al., 1995).

Sampling Methodology

Samples of host rock, mineralization and quartz veins were collected from the Tia Maria property from drill core, recirculation drilling chips and outcrop. Samples were collected from drill core CAD-001 from 0 m to 290 m depth, CAD-002 from 0 m to 231 m depth and CAD-003 from 0 m to 263 m depth. Recirculation drilling chips were taken from drill hole CARC-006 from 0 m to 170 m depth, CARC 007 from 0 m to 176m depth, CARC-0014 from 0 m to 192 m depth and CARC-0021 from 0 m to 182 m depth. Hand specimens were also collected from road-cuts and outcrops in the Cachuyo Zone of the Tia Maria property and from the nearby Lourdes, Rosa Maria, Cahuintala, Sauturno and Yanomayo epithermal veins.

Sampling of host rock from drill core was based on the core logs. The logs were studied to determine which intervals contained similar host rock lithologies and representative samples were taken. Samples of what were felt to be less altered (or unaltered where possible) equivalents of the rocks sampled from the drill core were taken from outcrops in and around the Cachuyo Zone.

Samples of mineralization taken from drill core and surface outcrop were selected on the basis of hand specimen characteristics (including the HCl acid test) that indicated copper content to obtain a representative suite. These minerals were black, blue, green, blue-green and brown and generally occurred as fracture fillings and coatings. Selection of recirculation drill holes and of specific 2 m intervals within them to be sampled was based on assay logs. The four highest-grade holes were selected and chips showing mineralization were collected from the intervals that assayed over 5000 ppm Cu.

Samples of Tia Maria quartz stockwork veins were taken from drill core. Samples from the various Rosa Maria type veins were taken from outcrop, except for a single sample where CAD-002 intersected what appeared to be this type of vein. Difficulties were encountered in determining field paragenetic relationships and sampling the Rosa Maria veins due to the fact that the accessible outcrops were largely mined out.

Sample Preparation and Analytical Procedures

Petrology

Petrographic analysis for host rock lithology and alteration characteristics was carried out on standard 30 mm thin sections (prepared by Spectrum Petrographics of Winston, Oregon) using water as a cover slip, on a polarized Olympus BH-2 microscope.

The identity of the mineralizing phases was determined using x-ray diffraction analysis (XRD) and electron microprobe analysis. XRD determines the identity of minerals through the use of the unique diffraction pattern created by x-rays passing through the minerals crystal structure. Amorphous mineraloids are not readily detectable by this method. Although semi-amorphous phases such as chrysocolla can produce a weak XRD signal, it may be completely overwhelmed by the presence of even minute amounts of clay mineral species. XRD analysis is also generally unable to detect any contaminant elements that may be included within the crystal lattices of a mineral, such as Cu substituting for manganese in pyrolusite (MnO_2).

Samples for XRD analysis were prepared by flaking or scraping off the oxide coating or encrustation of interest. Care was taken to obtain as pure a sample as possible and to avoid contamination from the underlying rock. The scrapings were then

ground to a fine powder in acetone with a mortar and pestle. The suspension was then spread on a glass slide using an eyedropper. After drying, the samples were analyzed at the New Mexico Bureau of Mines and Mineral Resources, in Socorro, New Mexico.

The XRD equipment was calibrated using the 111 silica peak at the beginning and end of each analytical session. All of the samples were scanned between 2° and 70° and analyzed using the JADE software and database. Once scanned, JADE was used to match the primary peaks with the most likely minerals contained within the Powder Diffraction File (PDF). All of the computer-matched peaks were compared to the ideal diffractograms for the matched minerals in the PDF by overlaying their peaks on the scan on the computer. In the case of unmatched peaks an extended peak report was performed by adding suspected minerals to the list of the computer matched phases and looking for high intensity peaks that match those in the scan. Again, the diffractograms were compared for accuracy.

Electron microprobe analysis determines the composition of a sample by bombarding a small area with an electron beam. The resulting X-ray emission is then detected and analyzed by a spectrometer. This spectrum gives the elemental composition and abundance of a substance, although not a specific formula. Electron microprobes analyze only the surface of a sample and most electron microprobes cannot detect elements lighter then oxygen or volatile phases such as water.

Samples for microprobe analysis were prepared by chipping off a small piece of rock bearing the oxide coating or encrustation of interest. These chips were then set in epoxy and allowed to set up over night. The epoxy "puck" was then ground down to expose the samples and then polished down to ~6 micron grit. Care was taken throughout to avoid grinding or polishing too deeply and removing the oxide coating.

Samples were then taken to the University of Utah in Salt Lake City, Utah, where they were carbon coated (for better conductivity) and analyzed using a CAMECA SX 50 electron microprobe.

The equipment was calibrated using hematite, pyrite, and cuprite standards prior to, twice during and after each analytical session. The elements silicon, copper, aluminum, phosphorus, iron and manganese were selected as being the most useful in determining the oxide mineralogy. Minerals were identified by comparing the weight percentages of each of the six elements obtained from the analysis to the percentages in stoichiometric mineral formulas.

Oxygen Isotope Mass Spectrometry

After crushing to -60/+80 mesh, oxygen was liberated from quartz and whole-rock samples using chlorine-trifluoride (ClF_3) and converted to CO_2 using the method of Clayton and Mayeda (1963) and Borthwick and Harmon (1982), with certain modifications to improve precision of the analyses: Pre-fluorination of quartz was replaced by hot vacuum pumping (150°C for 1 hour) of both quartz and whole rock samples to remove water or atmospheric moisture contamination in a consistent manner from both sample types; reaction temperature was increased to 550°C and; after a run was completed, the empty reaction vessels were once again hot vacuum pumped to destroy any iron oxide phases that may have formed during the preceding run (by reaction between hot ClF_3, oxygen and iron from the whole rock samples) and could potentially contaminate the following run.

Isotopic analyses were performed on a Finnigan MAT Delta E mass spectrometer using OZ-Tech gas standards with results reported as deviations from VSMOW using standard d-notation. NBS-28, used as a quartz $d^{18}O$ standard, was

analyzed 27 times with an average value of 9.1 per mil with a range of +/- 0.2 per mil (Appendix 7).

Fluid Inclusion Microthermometry

100 mm thick doubly-polished thin sections of the stockwork and gold bearing veins were prepared Mineral Optics Laboratory of Wilder, Vermont for fluid inclusion analysis. Thermometric analysis was performed on a Linkam THMS-600 heating/freezing stage, using an Olympus BH 2 microscope with 16 power oculars and a 40-power objective lens. Synthetic H_2O and CO_2 as well as potassium dichromate crystals were used to calibrate the stage. Accuracy is within +/- 0.1 ^{o}C at 0.0 ^{o}C and +/- 2 ^{o} C at 400 ^{o} C. The melting temperature of a synthetic H_2O inclusion was checked daily to ensure that the equipment remained calibrated. Due to the small size of the inclusions, a method of temperature cycling was utilized for both salinity and homogenization measurements. For salinity measurements, this entails slowly heating the frozen inclusion until the bubble moved slightly. The inclusion was then immediately cooled. If the bubble moved again with a few degrees, this meant that the ice had not totally melted as inclusions generally must be cooled at least 20 ^{o} C below their melting temperature in order for ice to re-nucleate. This cycle was repeated with increasing temperatures until a maximum melting temperature was obtained. A similar technique was used for homogenization temperature measurements. The inclusion was heated until the bubble appeared to vanish and at which point the inclusion was cooled. If the bubble reappeared within a few degrees, it had not homogenized, as inclusions generally must be cooled at least 20 ^{o} C below their homogenization temperature for the bubble to re-nucleate. This process was repeated with increasing temperature until a maximum homogenization temperature was obtained. The precision of this technique

was assessed by performing a duplicate homogenization and melting temperature measurement on each sample (Appendix 6). Homogenization temperatures were reproducible to within 3 °C and melting temperatures to within 0.2 °C. The Brown and Lamb equation in the program FLINCOR (Brown 1989) was used to obtain salinities, minimum trapping pressures and isochores from melting and homogenization temperatures.

Results

Host Rock Petrology and Alteration

Petrographic analysis of thin sections of samples taken from core and outcrop was carried out for host rock lithology and alteration characteristics. The samples analyzed displayed a wide range of degree of alteration, from almost complete replacement with virtually no relict textures (Fig. 4) to only moderate alteration with only incipient sericite formation (Fig. 5). Chloritization of mafic minerals was observed throughout. Rock names, based on thin section description and standard IUGS ternary diagrams, do not necessarily match those used during core logging (Fig. 6 and Appendix 1).

A granitic to granodioritic composition was confirmed for the rock described in the core logs as gneiss. Although in hand specimen crude banding of dark minerals is evident, in thin section evidence for a genuine Schlerin texture is less convincing. While there is a varying degree of segregation of mafic minerals, neither biotite nor hornblende shows any significant preferred orientation. The rocks logged as meta-granodiorite were determined to be a biotite monzogranite. Here, the segregation of mafics is weaker then in the previous examples, although it is still visible. These rocks are probably part of the Complejo Basal de la Costa.

Figure 4. Photomicrograph of typical sample showing well-developed alteration. What are interpreted to have originally been feldspars are > 80% replaced by sericite with an incipient argillic overprint. Upper picture is plain polarized light; lower is cross polarized.

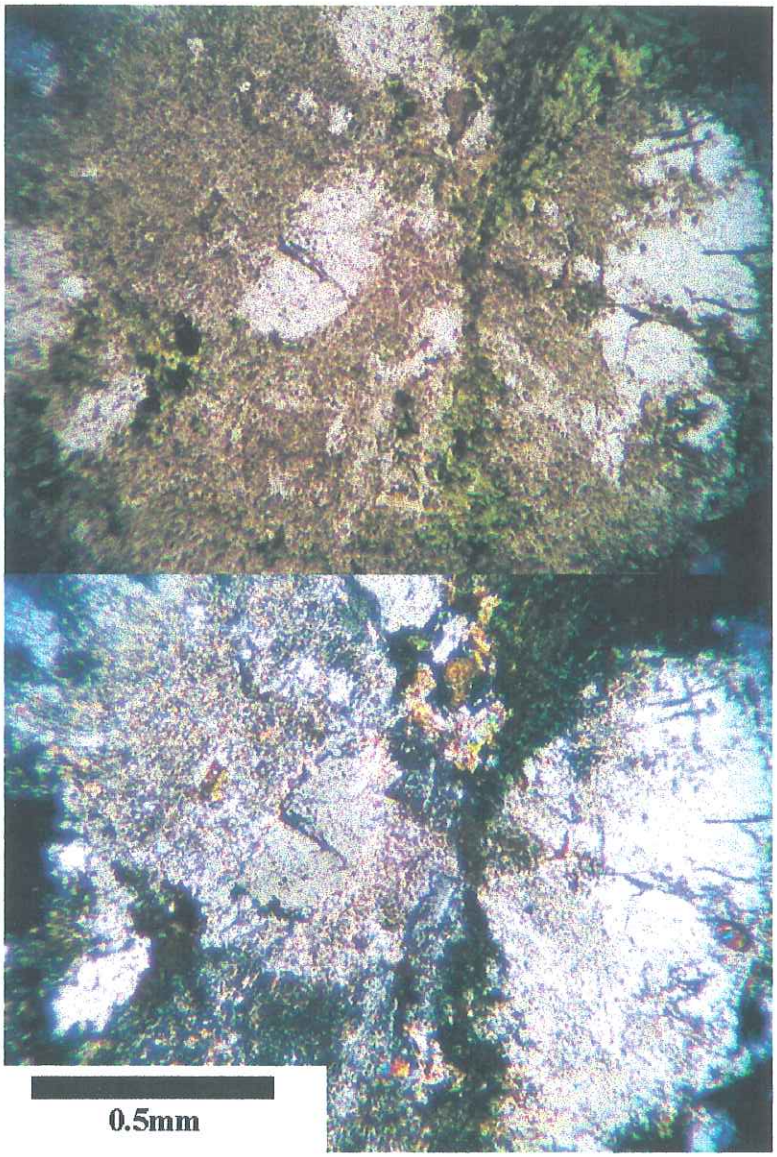
0.5mm

Figure 5. Photomicrograph of typical sample showing weakly-developed alteration. Plagioclase phenocryst displays incipient replacement by sericite along crystallographic boundaries and fractures. Upper picture is plain polarized light; lower is cross polarized.

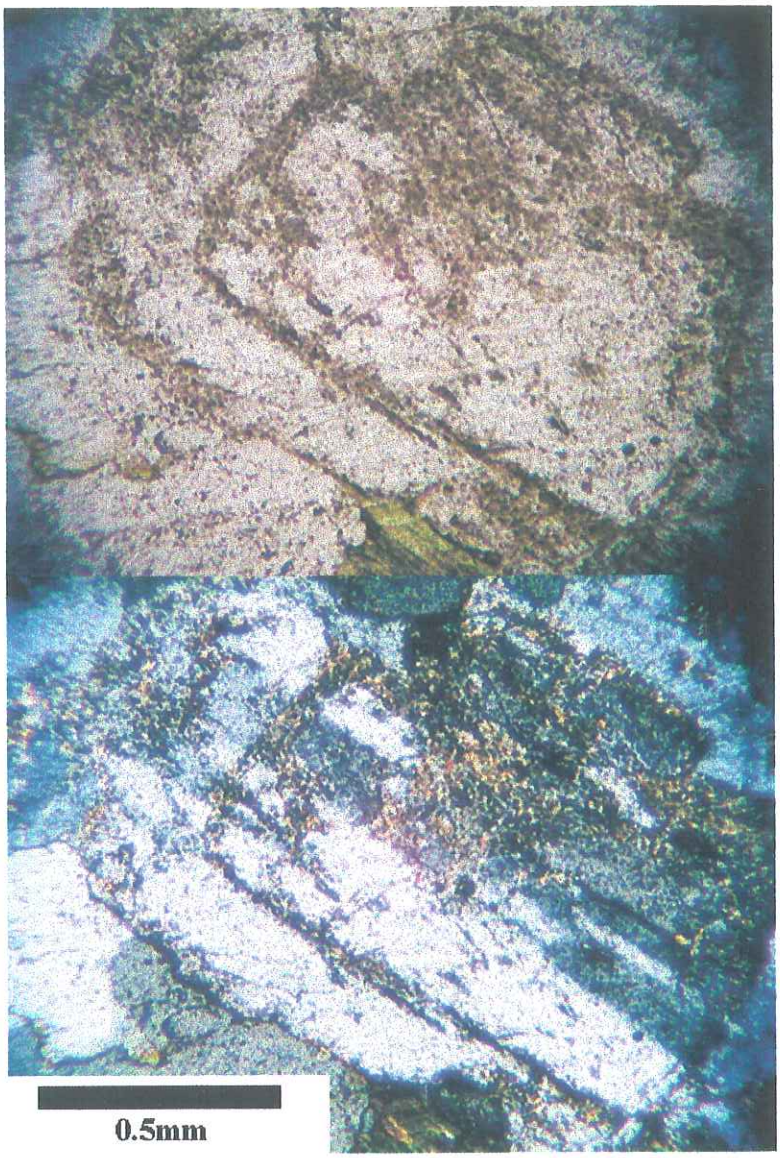
0.5mm

Figure 6. Samples analyzed by petrographic microscopy plotted on IUGS ternary diagrams. Upper diagram is for plutonic rock while lower is for volcanic rocks. Q, A and P stand for quartz, alkali feldspar and plagioclase feldspar, respectively. After LeMaitre (1989).

a - CAD-001 32.0 m
b - CAD-001 108.0 m
c - CAD-001 180.25 m
d - CAD-001 206.4 m
e - CAD-001 225.4 m
f - CAD-002 14.2 m
g - CAD-002 23.4 m
h - CAD-003 48.8 m
i - CAD-003 190.8 m
j - 0203481-8118741
k - 0204685-8118299
l - 02033370-8118975

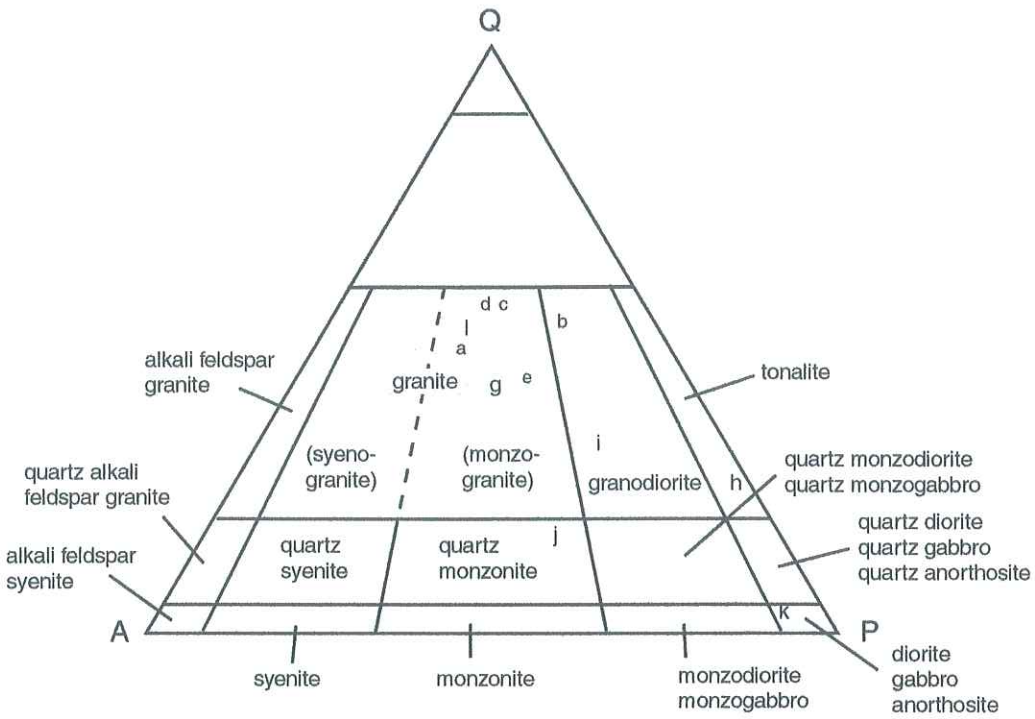
Q
d c
l
a
b
alkali feldspar granite
granite
g
e
tonalite
i
(syeno-granite)
(monzo-granite)
granodiorite
h
quartz monzodiorite
quartz monzogabbro
quartz alkali feldspar granite
quartz diorite
quartz gabbro
quartz anorthosite
alkali feldspar syenite
quartz syenite
quartz monzonite
j
k
A
P
syenite
monzonite
monzodiorite
monzogabbro
diorite
gabbro
anorthosite

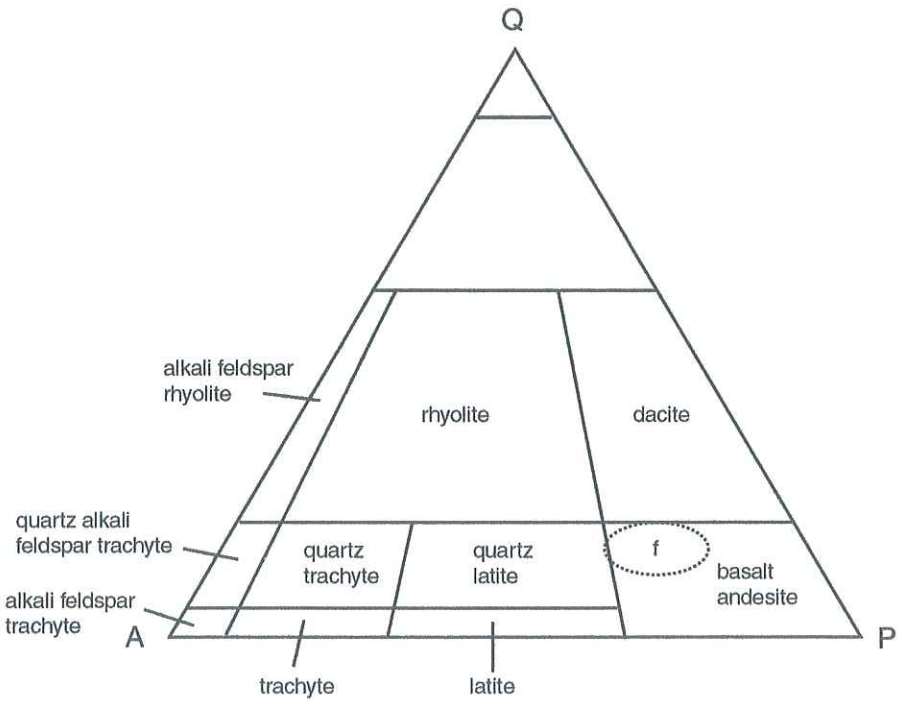
Q
alkali feldspar rhyolite
rhyolite
dacite
quartz alkali feldspar trachyte
quartz trachyte
quartz latite
f
basalt andesite
alkali feldspar trachyte
A
P
trachyte
latite

The original classification of the intervals logged as hornblende diorite porphyry was largely confirmed by petrographic microscopy. Some variation was noted in the proportions of biotite and hornblende as well as in the abundance of quartz, leading some samples to be classified as quartz-diorite. Some textural variation was also noted. While the quartz richer examples are more porphyritic, with euhedral plagioclase phenocrysts, the lower silica samples have predominantly equigranular plagioclase laths and therefore are best considered a biotite monzonite porphyry. These names match those assigned in the core logs. Noteworthy is the well-developed granophyric texture in the monzonite porphyry, which develops where plagioclase phenocrysts come into contact with the quartz + K-feldspar groundmass. The granitic rocks that lack banding are probably related to the Fiscal Pluton, a part of the Toquepala segment of the Coastal Batholith. A heavily altered, andesite porphyry was also examined and is likely a part of the Volcanico Toquepala group.

Alteration [classification based on the work of Rose and Burt (1979) and Reed (1997)] throughout is characterized by patchy K-silicate stable alteration, in the form of shreddy hydrothermal biotite, replacing magmatic biotite and minor mafic groundmass. This is overprinted by propylitic alteration in the form of chlorite $\pm$ rutile $\pm$ epidote $\pm$ magnetite that replaces a majority of the hornblende and magmatic biotite as well as some of the hydrothermal biotite. K-feldspar and to a greater extent plagioclase, are replaced to a greatly varying degree by fine white phyllosilicate, or "sericite," occasionally accompanied by silicification. As the mafic phases show greatly varying replacement by sericite and patches of granular quartz, ranging from incipient, to a replacement so complete that a tentative identification of the original mineral can only be made using the presence of clusters of rutile and magnetite. The degree of phyllic

alteration of the mafic phases broadly matches that of the feldspars. Finally, most samples show a faint argillic overprint, predominantly kaolinite, which mainly occurs in the groundmass and along the edges and crystal boundaries of the larger phenocrysts.

Supergene Oxides

A number of secondary oxide phases were identified in core and outcrop at Tia Maria (Appendix 2, 3 and 4). The major copper bearing phases are chrysocolla (a Cu/Fe/Al hydrous silicate mineraloid of variable composition) and malachite ($Cu_2CO_3(OH)_2$). Chrysocolla, which is an amorphous mineraloid of variable composition, ranges from a sky blue, aluminum bearing variety with a ~30 wt. % Cu content, to a darker blue variety with little or no aluminum with ~40 wt. % Cu. It mainly occurs as a fracture filling or a coating on other supergene fracture filling minerals. In outcrop and in near surface core, it is sometimes bleached almost white (Fig. 7). This is caused by leaching and results in an increased level of hydration and a Cu content of only 20 to 25 wt. %. Chrysocolla may also occur with a strong green or pink tint due to minor iron content or staining or mixing with clays. Malachite occurs as a fracture and box work filling, as a botryoidal encrustation in outcrop and sprays of small (~1mm) crystals growing on other fracture filling phases (Fig. 8).

Subsidiary copper bearing phases included pseudomalachite ($Cu_5(PO_4)_2(OH)_4$) and neotocite, a hydrous copper manganese iron silicate mineraloid of highly variable composition. Pseudomalachite occurs as sprays of green crystals in fractures, mimicking, as its name implies, the appearance of malachite; its Cu content is about 55 wt. %. Neotocite occurs mainly as black spots on fracture coatings. Its composition varies; for example, SiO_2 content varies from 15 to 30 wt. % and MnO_2 varies from less

Figure 7. Fracture surface with blue-green chrysocolla and black neotocite. Note bleaching at edges of chrysocolla. Paperclip approximately 3 cm long.

Figure 8. Fracture surface with sprays of green malachite crystals and spots of black neotocite. Paperclip approximately 3 cm long.

than 10 to almost 40 wt. %. Its Cu content varies from 30 to 37 wt. %. Neotocite is an iron-manganese-bearing analogue to chrysocolla (Titley and Chavez, 1999).

Microprobe analyses indicate that supergene hematite can contain up to 5 wt. % Cu. Although copper bearing hematite is not visually distinguishable from the regular variety, the copper content may sometimes be detected in hand specimen by use of an HCl/iron copper test. This involves putting a drop of dilute HCl on a fresh surface and rubbing a clean nail (or any other piece of clean steel/iron) in this slurry. If the sample contains oxidized Cu, a faint copper patina should will on the surface of the metal.

An unidentified, olive green to black, copper-iron-silicate, fracture coating phase was also investigated using microprobe. Its Cu content was determined to be 6 to 10 wt. %. However, as the total percentages of the six elements analyzed for (CuO, Fe_2O_3, MnO_2, P_2O_4, SiO_2 and Al_2O_3) did not add up to 100, this sample contains other elements that are unaccounted for and so the mineral cannot be identified.

Other fracture filling phases include berlinite ($AlPO_4$), goethite, kaolinite, illite and chlorite. Berlinite is a relatively rare (Foord et al, 1997) phosphate mineral that is isomorphous with quartz. It has been identified as a supergene mineral associated with hematite, in the oxidized zones of porphyry copper deposits in Arizona (Anthony et al, 1995). Although in its pure form it is pale pink to gray with a vitreous luster, it more often occurs in nature as massive or grainy with a brown color that is most likely attributable to iron staining.

Quartz Veins

A petrographic survey was taken of the doubly polished fluid inclusion wafers before thermometric analysis was carried out. The results from the Tia Maria veins, whether or not containing sulfide mineralization (or its oxidation products), were

broadly similar. The veins are over 90% anhedral quartz up to 0.5mm in size (Fig. 9). Extinction ranges from uniform to slightly undulatory. Rutile needles are fairly common and wall rock inclusions occur. The quartz crystals all show evidence of fracturing and planes of secondary inclusions are very abundant. Patches or bands of very fine quartz with rounded edges and highly undulatory extinction occur, but appear to be the result of shearing, possibly caused by the reactivation of the fault/fracture that hosts the vein. Recrystalization seems to have occurred here as this quartz does not have the planes of secondary inclusions that characterize the rest of the vein quartz. Secondary hematite, which appears to replace primary sulfides, occurs in varying quantities, ranging from the occasional crystal to a solid band running through the vein. Regardless of its abundance, it always occurs at a paragenetically late stage, in the center of the veins. Patches and veinlets of chlorite with no particular paragenetic relationship make up to ~10% of the vein and appear to be alteration related. No vugs or open spaces occur within the stockwork veins other then those due to the weathering out of sulfides.

The Rosa Maria type veins have a significantly different texture then the Tia Maria stockwork veins, although they are still dominated by quartz. The quartz is characterized by euhedral, bladed crystals up to 2 mm long. Growth bands of fluid inclusions occur in a chevron pattern (Fig. 10). Extinction is uniform throughout. Vugs and open spaces are abundant. The veins are associated with abundant hematite and some chrysocolla, both of which are likely the result of oxidation of primary sulfides. Fine disseminated gold occurs within the masses of dark red to black secondary hematite (Dave Andrews, pers. com. 1999). Some of the hematite, in the form of specularite crystals up 1 cm across, appears to be primary.

Figure 9. Photomicrograph of Tia Maria quartz vein. Note patches of chlorite. Upper picture is plain polarized light while lower is cross polarized. Strong interference colors caused by thickness of fluid inclusion section.

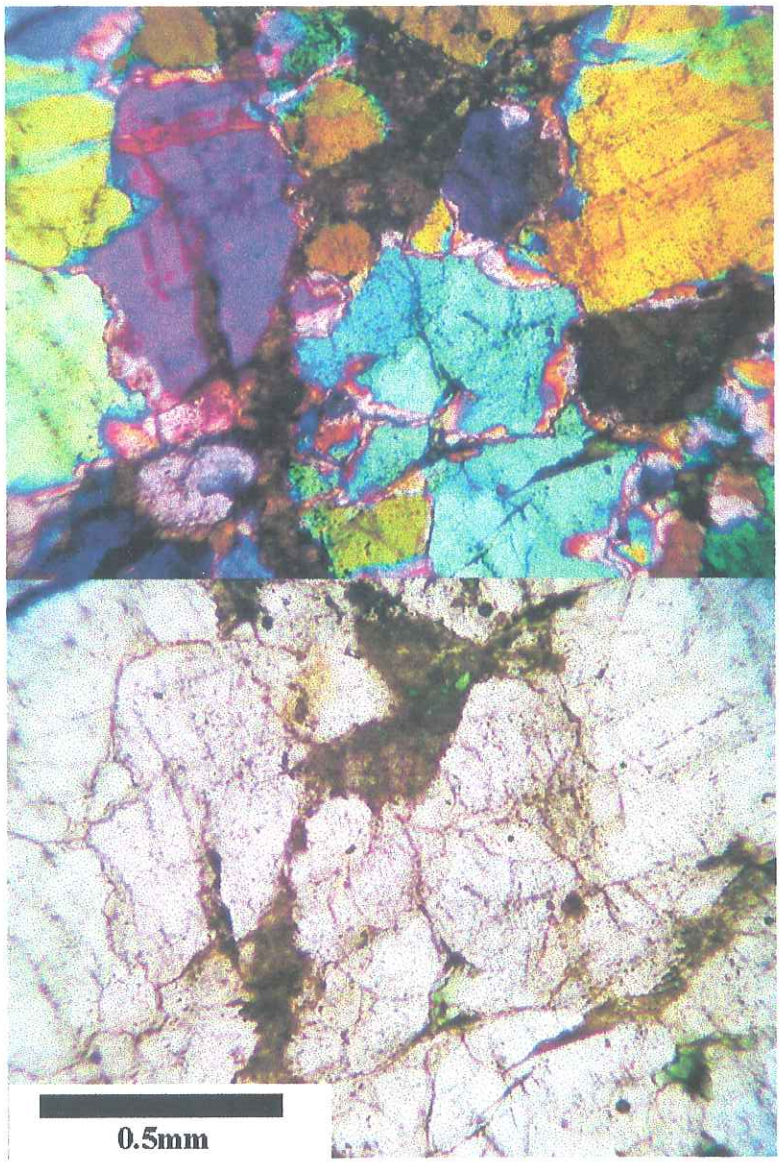
0.5mm

Figure 10. Photomicrograph of Rosa Maria-type quartz vein. Note euhedral, bladed crystals and growth banding. Upper picture is plain polarized light while lower is cross polarized. Strong interference colors caused by thickness of fluid inclusion section.

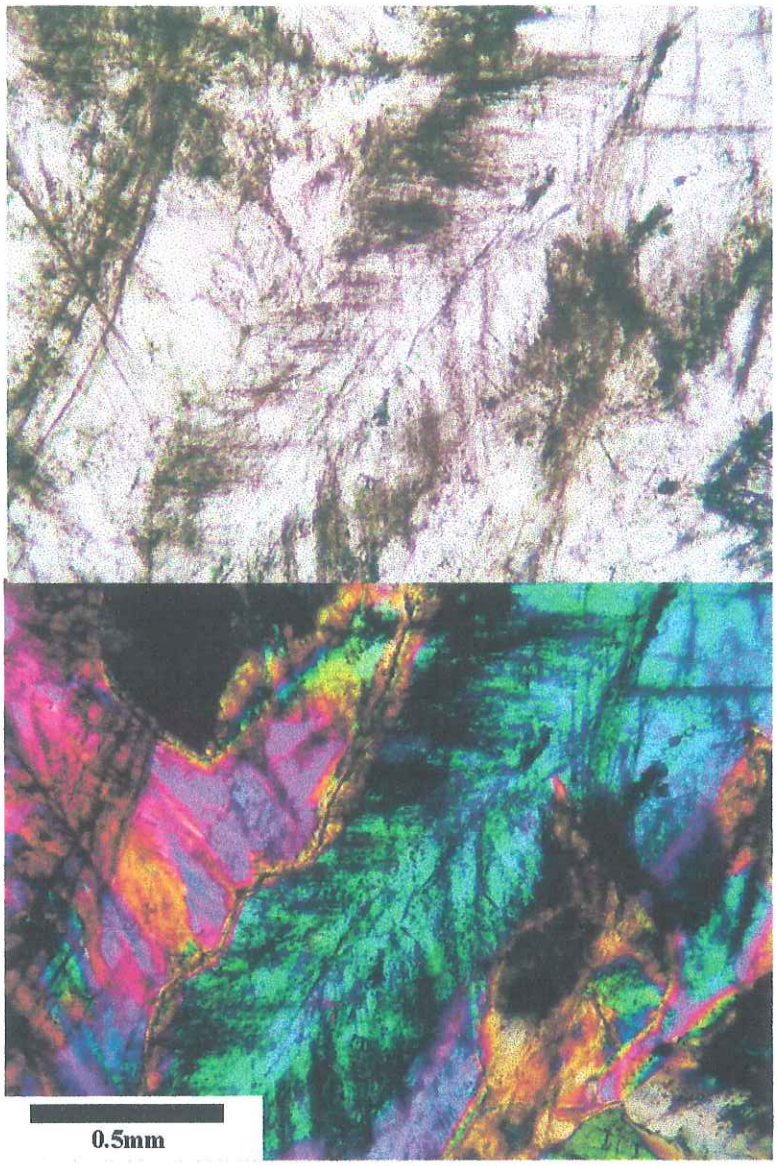
0.5mm

Fluid Inclusions

A fluid inclusion study was carried out on samples of the Tia Maria stockwork and Rosa Maria quartz veins to estimate the temperature and salinity of the mineralizing fluids and to calculate their oxygen isotope composition.

Primary inclusions in the Tia Maria veins were dominantly two phase (liquid + vapor) and ranged in size from 2 to15 mm with most being less then 8 mm. Less then 5 % contained a trapped mineral. No CO_2 phase was visible. The degree of liquid fill (F) ranged from very liquid rich (F = 0.99) to those containing relatively more vapor (F = 0.80). Homogenization of the bubble to the liquid phase occurred at temperatures ranging from 323 to 397 °C and averaged 360 °C (Fig. 11 and Appendix 5). No correlation was found with depth. Salinity measurements were performed on 57 of the larger primary inclusions. Smaller inclusions could not be measured, as the vapor bubbles did not exhibit sufficient movement on ice melting. No salinity measurements were obtained from CAD 001 108 for this reason. Salinities ranged from 3.6 to 13.1 eq. wt. % NaCl, with an average of 7.7 eq. wt. % NaCl (Fig. 12). No significant Th versus salinity trend was found (Fig. 13).

For comparison, thermometric analysis was also carried out on secondary inclusions. All the Tia Maria veins have similar secondary inclusions, with homogenization temperatures ranging from 190.8 to 259.8 °C, with an average of 233.5 °C. Salinities ranged from 3.1 to 11.6 eq. wt. % NaCl, with an average of 7.1 eq. wt. % NaCl.

A second group of secondary inclusions was documented in CAD 001 108 that does not appear to occur in the other samples. Homogenization temperatures of these

Figure 11. Fluid inclusion homogenization temperatures.

11 a - Cummulative chart of all inclusion homogenization temperatures.
11 b - CAD-002-46.9 m
11 c - CAD-002-86.5 m
11 d - CAD-002-87.5 m
11 e - CAD-001-108.0 m
11 f - CAD-002-123.0 m
11 g - CAD-002-194.5 m
11 h - CAD-003-263 m

Figure 11a

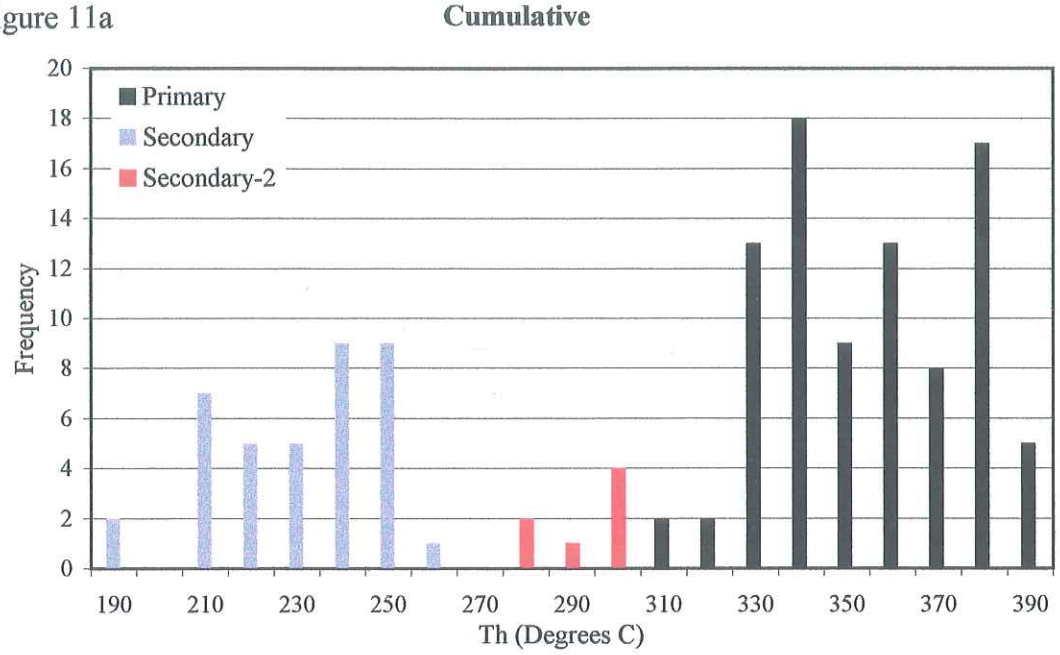
Cumulative
Primary
Secondary
Secondary-2
Frequency
0
2
4
6
8
10
12
14
16
18
20
190
210
230
250
270
290
310
330
350
370
390
Th (Degrees C)

Figure 11b

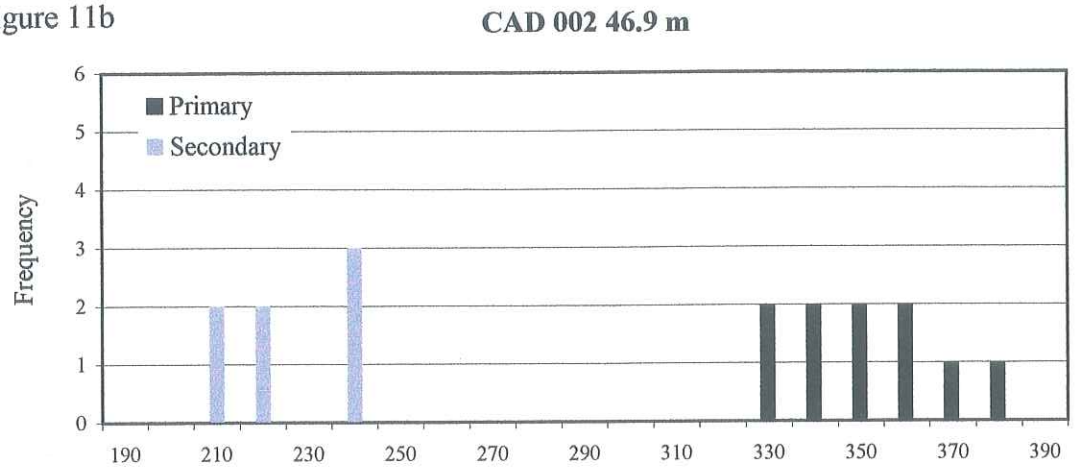

Figure 11c

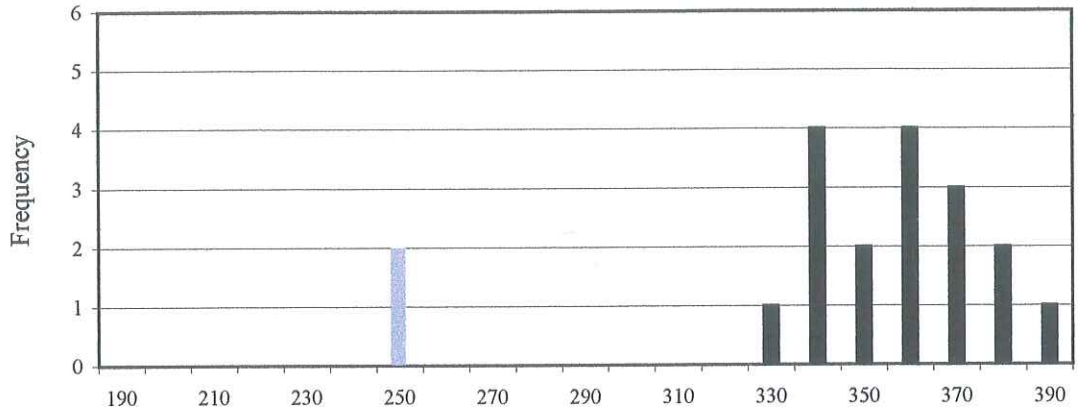

Figure 11d

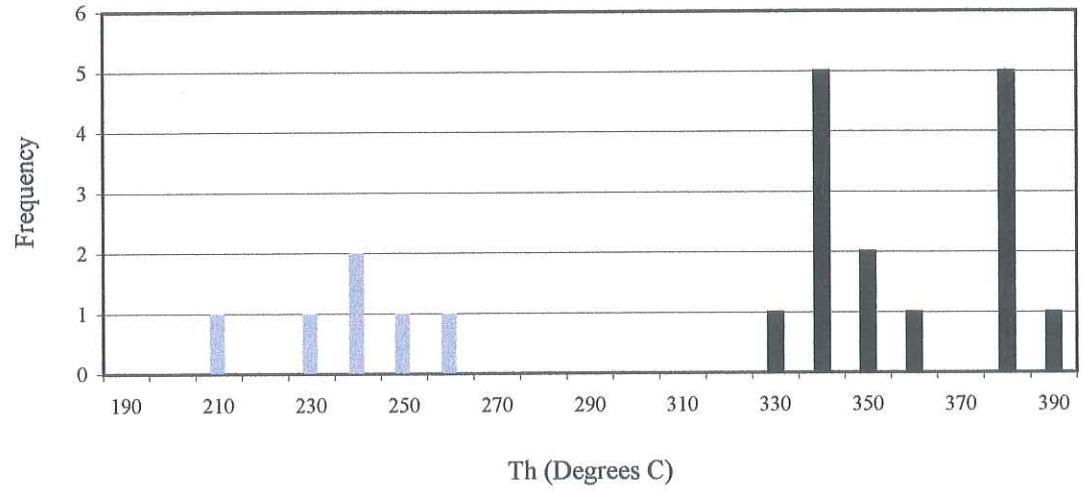

Figure 11e

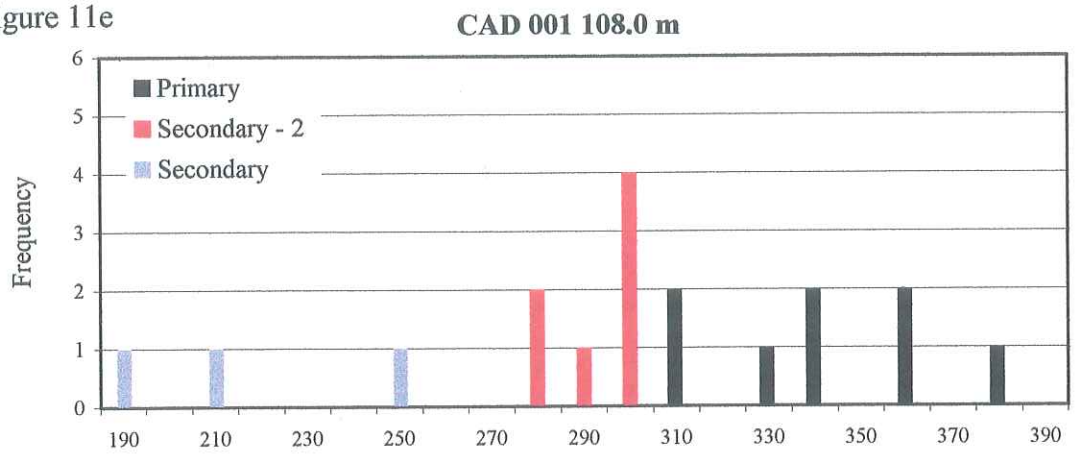

Figure 11f

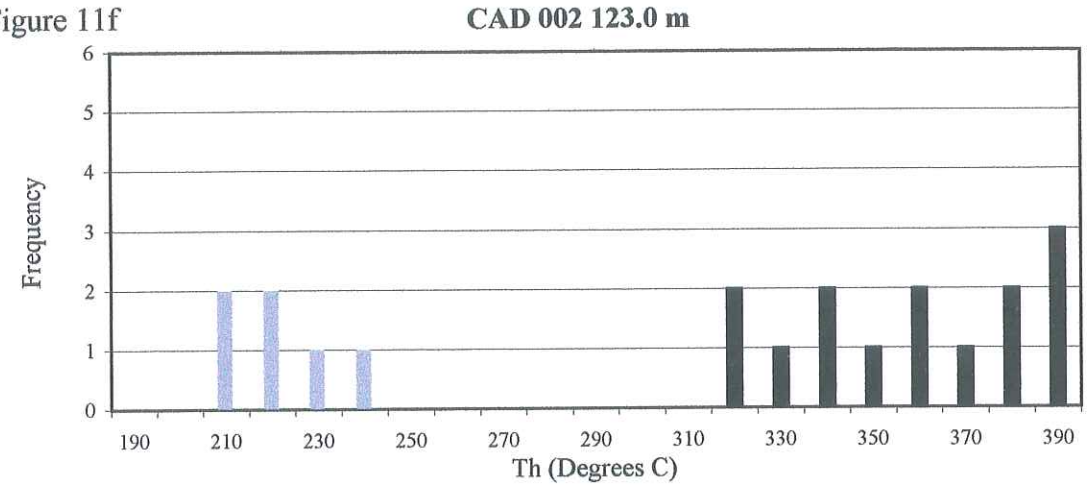

Figure 11g

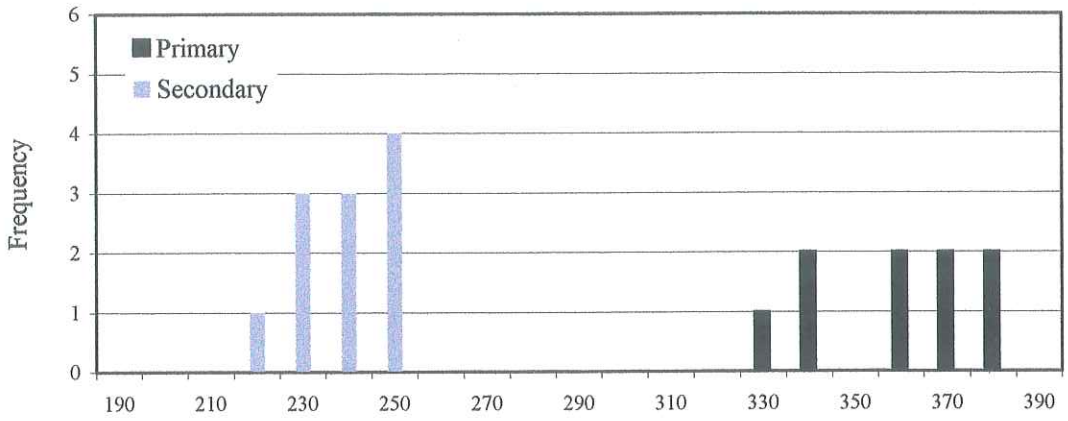

Figure 11h

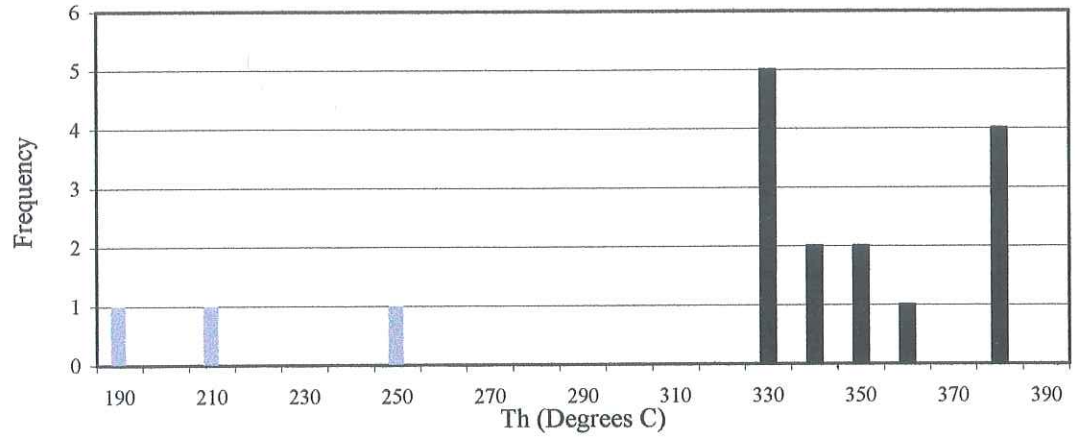

Figure 12 . Fluid inclusion salinities.

12 a - Cummulative chart of all inclusion homogenization temperatures.
12 b - CAD-002-46.9 m
12 c - CAD-002-86.5 m
12 d - CAD-002-87.5 m
12 e - CAD-001-108.0 m
12 f - CAD-002-123.0 m
12 g - CAD-002-194.5 m
12 h - CAD-003-263 m

Figure 12a

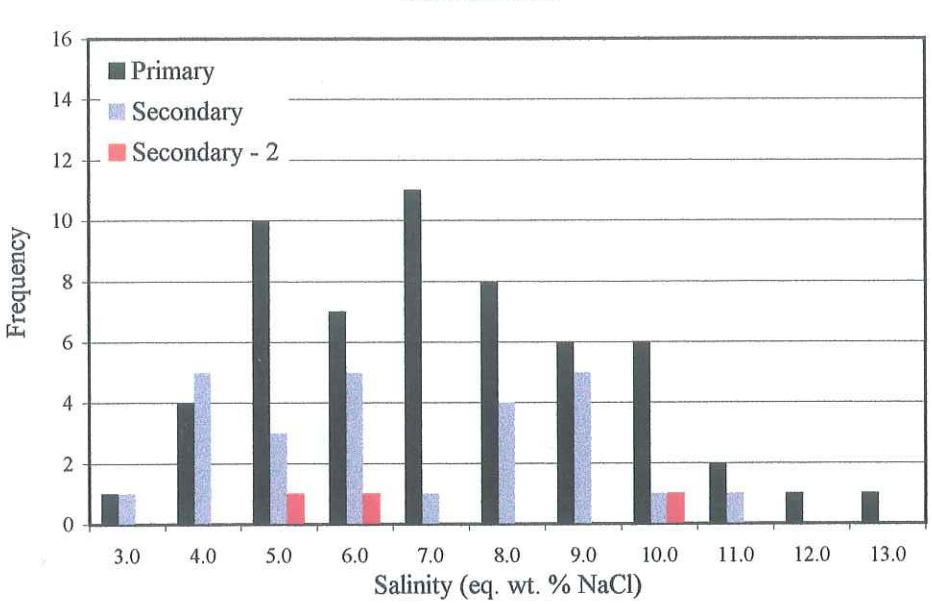
Cumulative
Primary
Secondary
Secondary - 2
Frequency
16
14
12
10
8
6
4
2
0
3.0
4.0
5.0
6.0
7.0
8.0
9.0
10.0
11.0
12.0
13.0
Salinity (eq. wt. % NaCl)

Figure 12b

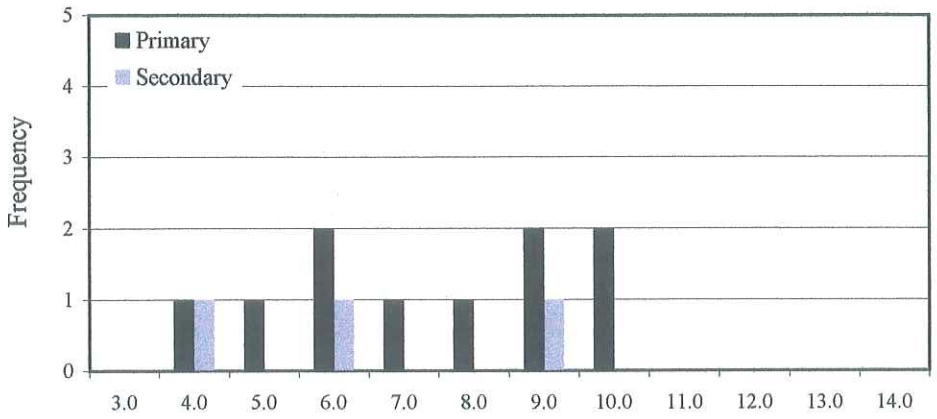

Figure 12c

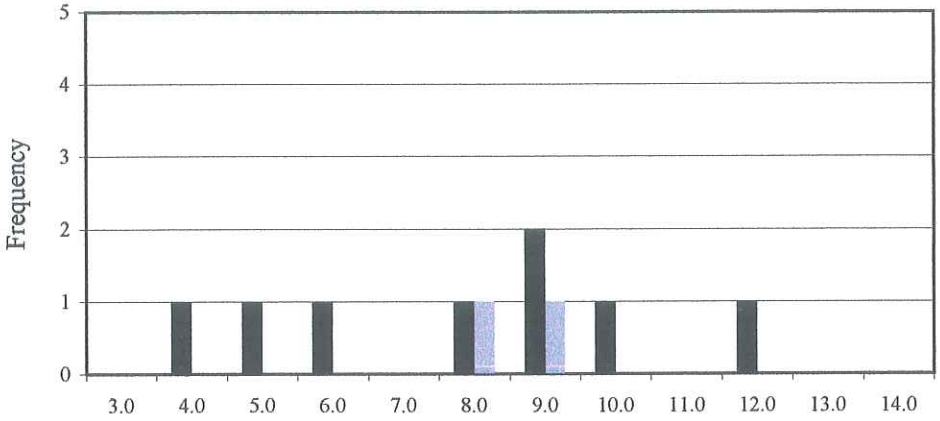

Figure 12d

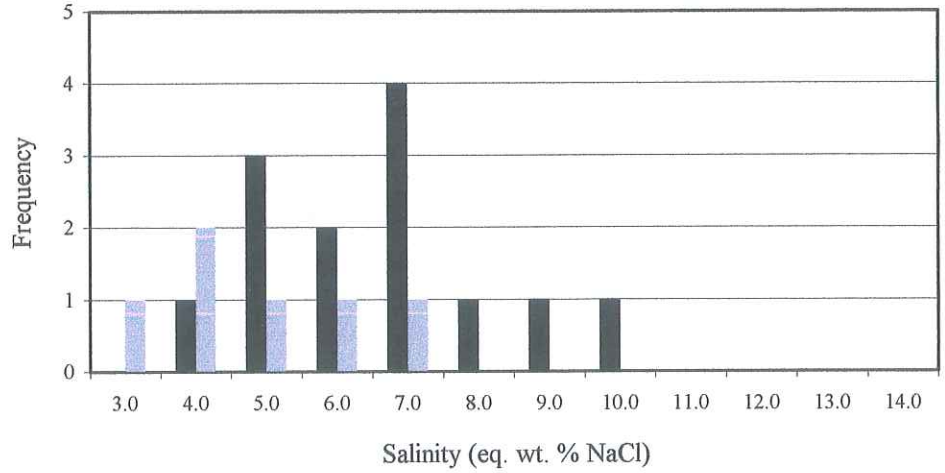

Figure 12e **CAD 001 108.0 m**

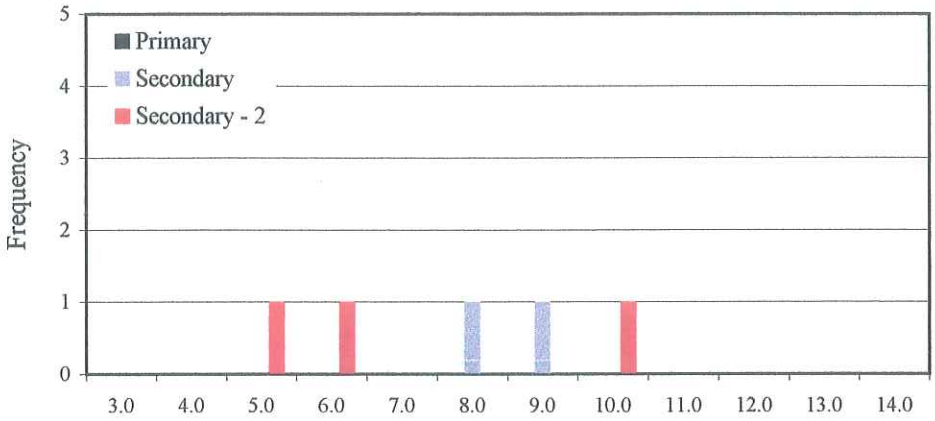

Figure 12f **CAD 002 123.0 m**

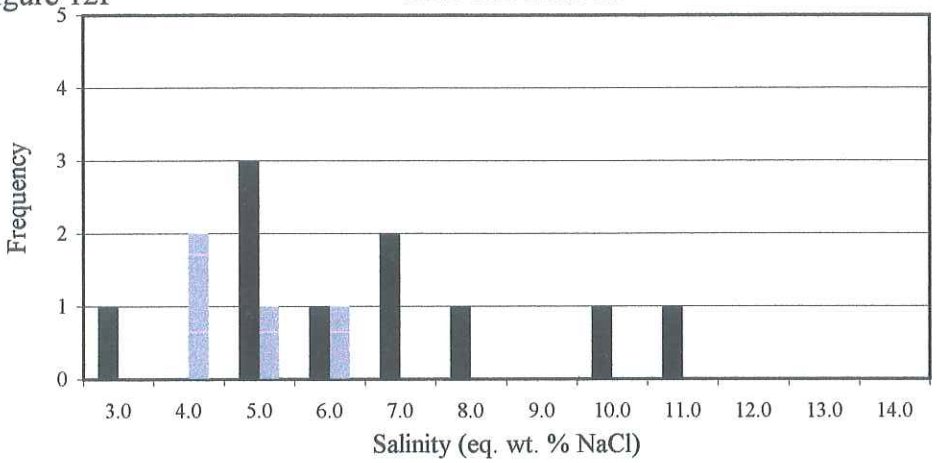

Figure 12g

CAD 002 194.5 m

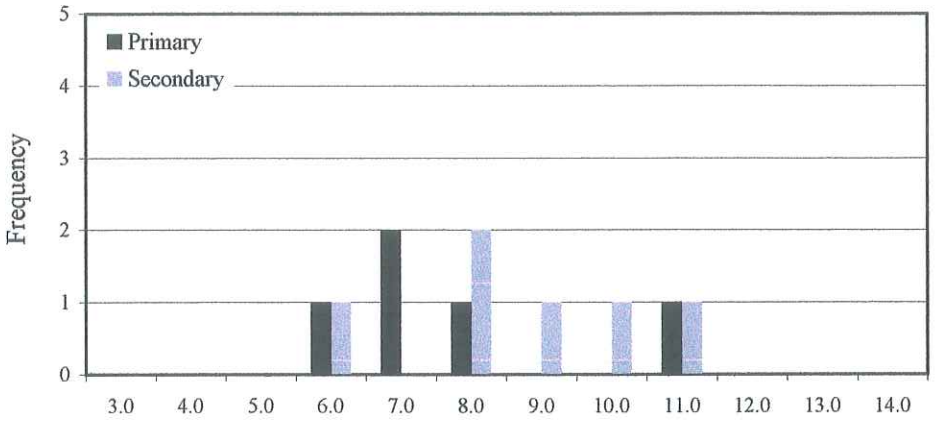

Figure 12h

CAD 003 263 m

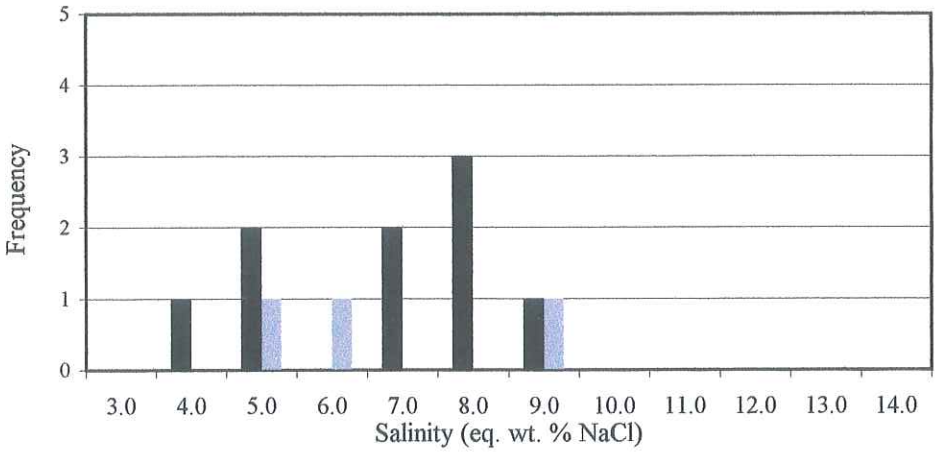

Figure 13. Plot of fluid inclusion homogenization temperature vs. salinity. Upper group is primary while lower group is secondary.

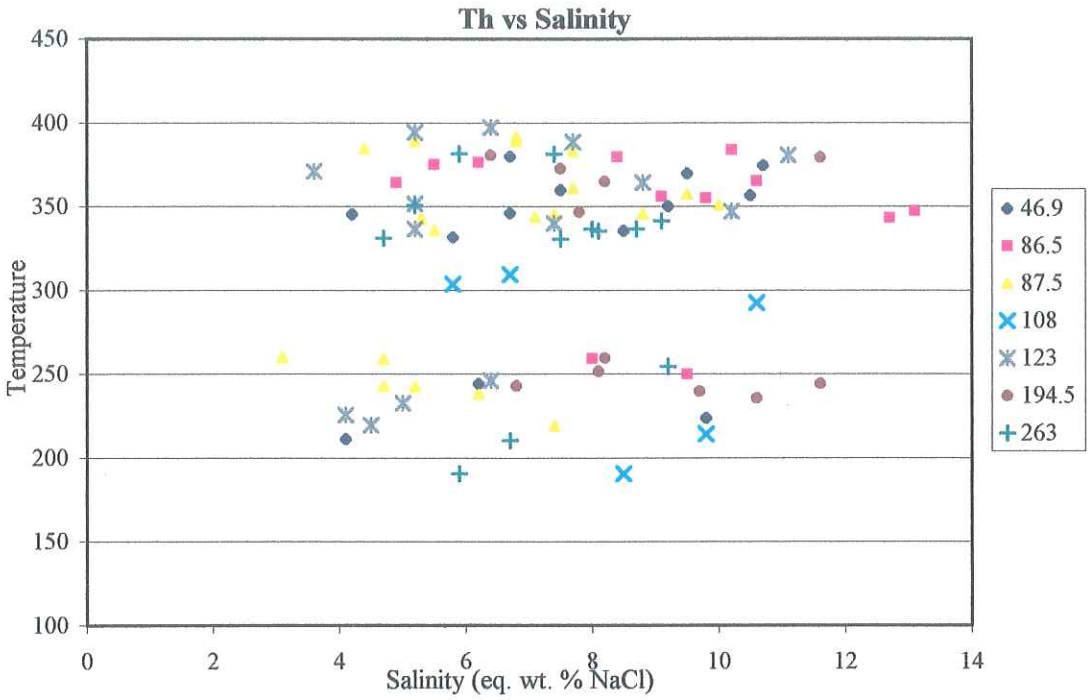
Th vs Salinity
450
400
350
300
250
200
150
100
Temperature
0
2
4
6
8
10
12
14
Salinity (eq. wt. % NaCl)
46.9
86.5
87.5
108
123
194.5
263

inclusions ranged from 283.2 to 318.4 °C, with an average of 301.8 °C. Salinities ranged from 4.8 to 10.6 eq. wt. % NaCl, with an average of 7.7 eq. wt. % NaCl.

There were two types of primary inclusions in the Rosa Maria veins: liquid dominated and vapor dominated. Their occurrence in the same growth bands suggests that they formed in equilibrium, and therefore the fluid was undergoing phase separation, or boiling. Neither trapped minerals nor a CO_2 phase were visible. The very small size of the inclusions (< 1 mm) in the Rosa Maria veins led to difficulties in obtaining measurements. As temperature was increased, the vibration of the by then 0.1 mm vapor bubble became indistinguishable from the vibration of the sample itself, leading to a large uncertainty in the temperature of homogenization. Use of the cycling method faced the inability to exactly determine when the vapor bubble renucleated. Several approximate measurements of homogenization temperature were made on 6, larger than average, liquid dominated inclusions in a sample of the Rosa Maria vein, giving a range of 250 to 280 °C. Melting temperatures were unobtainable.

Stable Isotopes

A total of 10 Tia Maria stockwork vein samples, 7 Rosa Maria quartz vein samples (Table 1) and 10 whole-rock samples (Table 2) were analyzed for $d^{18}O$. The $d^{18}O$ value of the Tia Maria quartz veins averaged 9.0 ‰, with a range of 0.9 ‰. The Rosa Maria veins averaged 12.3 ‰, with a rather larger range of 4.9 ‰.

Whole-rock $d^{18}O$ analyses were carried out on ten samples of altered rocks from core and from less altered rocks taken from surrounding outcrops. Most of the samples, whether the granitoids, diorites or the andesite porphyry fell into a $d^{18}O$ range of 8.5 to 9.5 ‰. Two samples, a banded granite and a monzonite porphyry which were collected from outcrop at some distance from the drill holes (at what is felt to be the

Table 1
Oxygen Isotope Analysis of Quartz.

Location	Name/Rock Type	$d^{18}O$ (quartz) $^{o}/_{oo}$
	Tia Maria	
CAD-003-127	drill core	9.0
CAD-002-213.4	drill core	8.9
CAD-002-86.5	drill core	9.0
CAD-001-108	drill core	8.4
CAD-001-97.4	drill core	9.3
CAD-003-263	drill core	8.8
CAD-002-87.5	drill core	9.0
CAD-002-194.5	drill core	9.2
CAD-002-46.9	drill core	9.2
CAD-001-129.2	drill core	9.2
	Rosa Maria	
0206028-8116707	West Yanomayo	15.1
0202449-8118174	Lourdes	13.8
0207036-8116761	Yanomayo	13.0
0202782-8115360	Cahuintala	10.2
0201892-8117092	Rosa Maria	11.0
0204651-8117885	Saturno	11.1
CAD-001-104	drill core	11.8

Table 2
Oxygen Isotope Whole Rock Analysis

Location	Name/Rock Type	$d^{18}O$ $^{o}/_{oo}$
CAD-001-102.4	andesite dyke	6.8
CAD-001-110.6	granodiorite	8.9
CAD-001-140.5	hornblende quartz-diorite porphyry	8.5
CAD-002-14.2	andesite porph	8.7
CAD-002-26.8	granodiorite	9.2
CAD-002-213.4	meta-granodiorite	8.4
CAD-003-48.9	quartz-diorite porphyry	9.3
0204685-8118299	hornblende biotite diorite porphyry	9.3
0203370-8118795	banded granite	11.4
0203481-8118741	biotite quartz-monzonite porphyry	10.7

core of the system) had values of 11.36 and 10.70 $^{o}/_{oo}$ respectively. The crosscutting andesite dyke had a $d^{18}O$ of 6.85 $^{o}/_{oo}$.

Discussion

Supergene Mineralization

Supergene copper mineralization at Tia Maria is dominated by chrysocolla, malachite and pseudomalachite. Using the stability diagrams of Vink (1986) for malachite and of Magalhaes et al. (1986) for pseudomalachite, it is possible to constrain the conditions of oxidation (Fig. 14 and 15). Assuming a P_{CO2} of $10^{-3.5}$ atm, a typical atmospheric concentration, and a copper concentration of 10^{-6} molal (Vink, 1986), a pH of ~7 and an Eh of ~0.6 to 0.8 can be established. Being a mineraloid and not a mineral, chrysocolla does not have a well-constrained stability field, although it tends to form under less acid conditions (Newberg, 1967; Chavez 2000).

Melchiorre et al. (1999 and 2000) conducted a $d^{18}O$ and $d^{13}C$ study of malachite and azurite (which forms in very similar conditions to malachite; see figure 16) which indicated that unless the minerals were forming directly on a carbonate rock or in a carbonate saturated environment such as a cave, the carbon and oxygen is derived from atmospheric CO_2. As there is a complete absence of any carbonates in the Tia Maria area, it is felt that the malachite likely formed by the later method.

The source of the phosphate in pseudomalachite and berlinite is somewhat more speculative. The usual source would be from accessory apatite in the host intrusive. However, petrographic examination of neither altered nor relatively unaltered Tia Maria samples yielded any apatite. Assuming that supergene oxidation at Tia Maria occurred in the late Oligocene and Miocene, which would be contemporaneous to the nearby porphyries in the Toquepala region and the more distant Chilean deposits of

Figure 14. Eh - pH malachite - azurite stability diagram. Note mineralogical dependence on P_{CO2} concentration. After Vink (1986).

Figure 15. Log Cu activity - pH copper phosphate stability diagram. After Magalhaes et al. (1986).

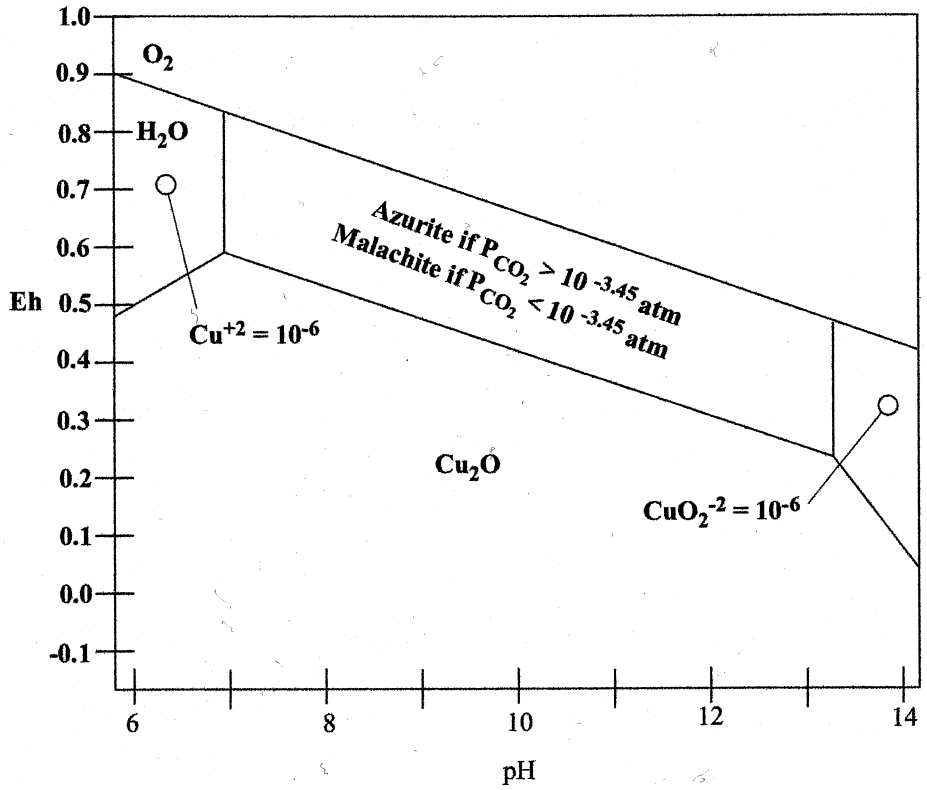
1.0
0.9
0.8
0.7
0.6
0.5
0.4
0.3
0.2
0.1
0.0
-0.1
Eh
O_2
H_2O
Azurite if $P_{CO_2} > 10^{-3.45}$ atm
Malachite if $P_{CO_2} < 10^{-3.45}$ atm
$Cu^{+2} = 10^{-6}$
Cu_2O
$CuO_2^{-2} = 10^{-6}$
6
8
10
12
14
pH

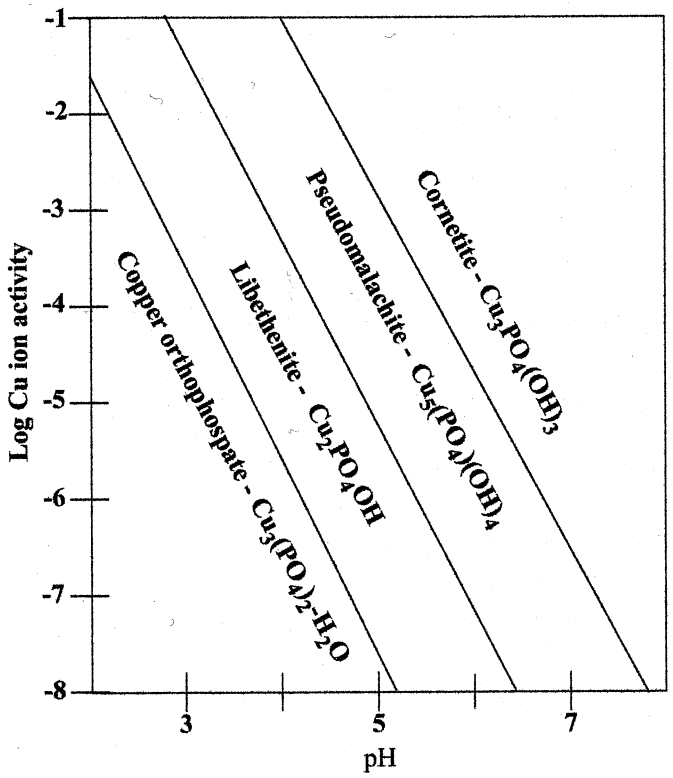
-1
-2
-3
-4
-5
-6
-7
-8
Log Cu ion activity
Cornetite - $Cu_3PO_4(OH)_3$
Pseudomalachite - $Cu_5(PO_4)(OH)_4$
Libethenite - Cu_2PO_4OH
Copper orthophospate - $Cu_3(PO_4)_2$-H_2O
3
5
7
pH

Chuquicamata, La Escondida and the Copiapo district (Clark et al., 1990b), a biogenic source may be postulated. Then, as now, Tia Maria was on the coast and the area may easily have hosted a sizable bird population. Economic aluminum phosphate deposits are known to have formed from the guano of Tertiary sea-fowl colonies by reaction with granitic bedrock (eg., Fuller, 1979). At the Saldanha Bay deposits in South Africa, it is noted that some brown vein filling phosphate minerals occur with and replace clays derived from oxidation of host granites, which is similar to the style of occurrence of berlinite and pseudomalachite noted at Tia Maria.

This assemblage of supergene minerals and its occurrence as a product of quasi-*in situ* oxidation (ie, no leached cap, fracture control, no enrichment blanket) at Tia Maria can also be used to make inferences about the hypogene mineralization. Based on the diagram from Chavez (2000) illustrating the paragenesis of copper oxide minerals, the protore was dominated by chalcopyrite. The proportion of copper to iron sulfides may have been five to one or more. A greater amount of pyrite would have resulted in more sulfuric acid during supergene alteration and a lower pH assemblage (Titley and Marozas, 1995; Chavez, 2000).

Fluid Inclusions

Isochores calculated for the primary inclusions give a pressure/temperature (bars/^{o}C) slope of ~10:1, indicating a low pressure dependence (Fig. 16). The data gathered from the Tia Maria quartz veins showed two-phase, liquid dominated fluid inclusions with homogenization temperatures averaging ~360 ^{o}C and salinities of ~8 eq. wt. % NaCl and a corresponding minimum trapping pressure of 200 to 300 bars.

The salinity of the aqueous phase that first exsolves from a crystallizing magma is thought to range from 5 to 12 eq. wt. % NaCl (Burnham, 1979). The typical model

Figure 16. Calculated minimum trapping pressures vs. homogenization temperatures. Plotted isochores (lines of equal density) are samples from representative primary inclusions.

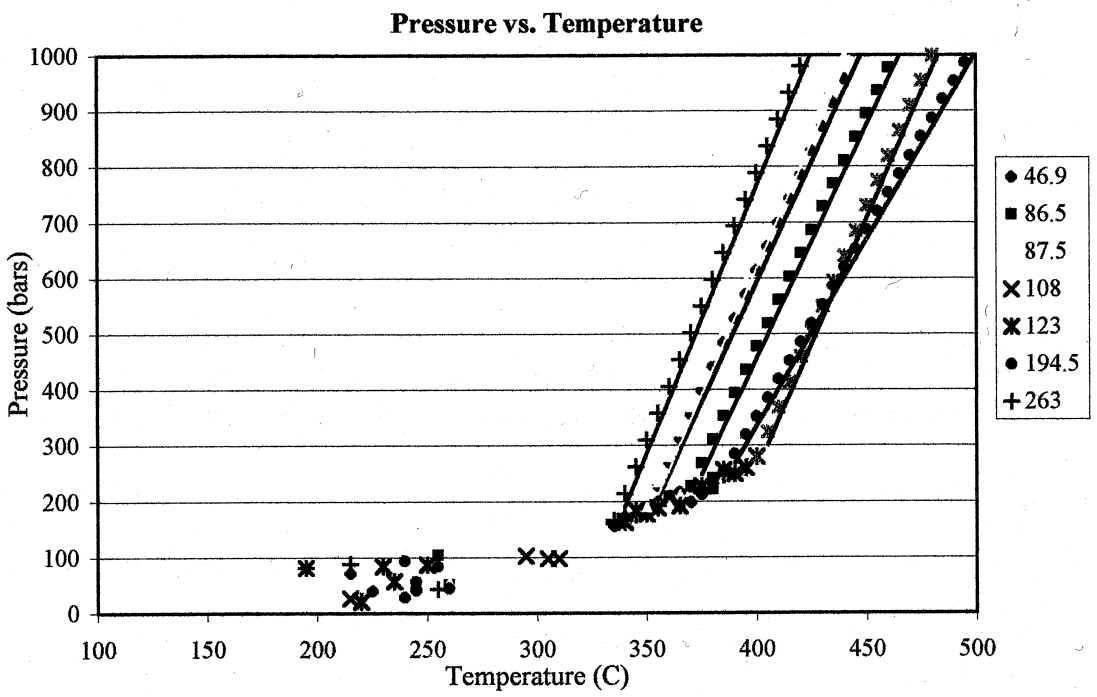
Pressure vs. Temperature
Pressure (bars)
1000
900
800
700
600
500
400
300
200
100
0
100
150
200
250
300
350
400
450
500
Temperature (C)
46.9
86.5
87.5
108
123
194.5
263

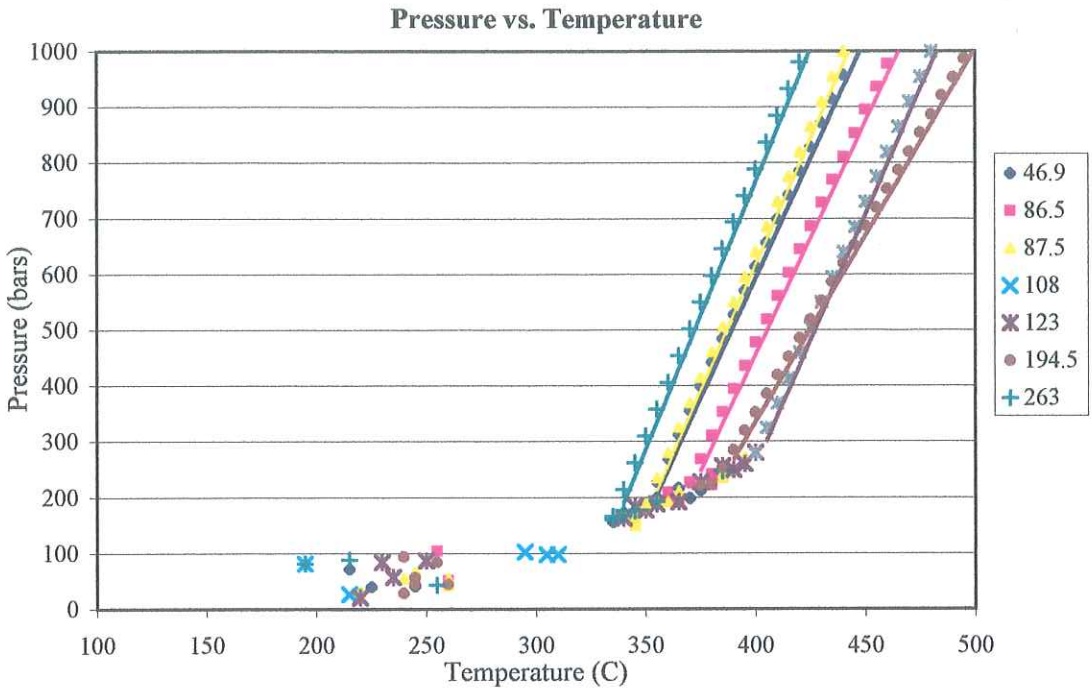
Pressure vs. Temperature
Pressure (bars)
1000
900
800
700
600
500
400
300
200
100
0
100
150
200
250
300
350
400
450
500
Temperature (C)
46.9
86.5
87.5
108
123
194.5
263

of such a system (eg. Hedenquist and Lowenstern, 1994; Cline, 1995; Burnham, 1997) envisions that as this fluid rises and temperatures and pressures decrease, the fluid will separate into immiscible low salinity vapor and high salinity brine phases. In lower pressure systems, this phase separation may occur immediately during exsolution from the melt. Coexisting low salinity vapor dominated and high salinity liquid dominated fluid inclusions are, in fact, commonly observed in porphyry copper deposits (eg. Roedder 1984; Dilles and Einaudi, 1992; Bodnar, 1995). However, this evidence of boiling is only rarely seen in the propylitic zone of a porphyry copper (Beane and Bodnar, 1995; Roedder and Bodnar, 1997), the inclusions instead typically having salinities of ~10 to 20 eq. wt. % and homogenization temperatures of 200 to 350 °C (Rose and Burt (1979); Reed (1997).

The P-T path that a mineralizing fluid could take, cooling and decompressing from the relatively high pressures and temperatures of its source at the edges of a crystallizing magma body, can be seen by examining the temperature-composition diagrams, modified after Bowers and Helgeson (1983), for the system H_2O-NaCl, at varying pressures (Fig. 17). The diagrams trace the evolution of a magmatic aqueous fluid of 12 eq. wt. % NaCl (a salinity equivalent to the more saline of the Tia Maria fluid inclusions) evolved from the solidus boundary of a relatively deep (~8 km) granodiorite porphyry stock, as hypothesized by Burnham (1979), at a temperature of ~700 °C and a pressure of ~2 kbar. Throughout its P-T evolution, the magmatic aqueous phase stays in the liquid field without undergoing phase separation.

The typical copper porphyry models mentioned above suggest that the metals are transported in solution by the high salinity brines. The ~8 eq. wt. % NaCl average salinity of the Tia Maria inclusions is significantly lower then that of the brines.

Figure 17. P-T evolution of a magmatic aqueous fluid of 12 eq. wt. % NaCl evolved from the solidus boundary of a relatively deep (~8 km) granodiorite porphyry stock, as hypothesized by Burnham (1979), at a temperature of ~700 ^{o}C and a ~ 2 kbar pressure. Note that through its evolution, the magmatic aqueous phase stays in the liquid field without undergoing phase separation. Modified after the H_2O-CO_2 system temperature-composition diagrams, at varying pressures, of Bowers and Helgeson (1983).

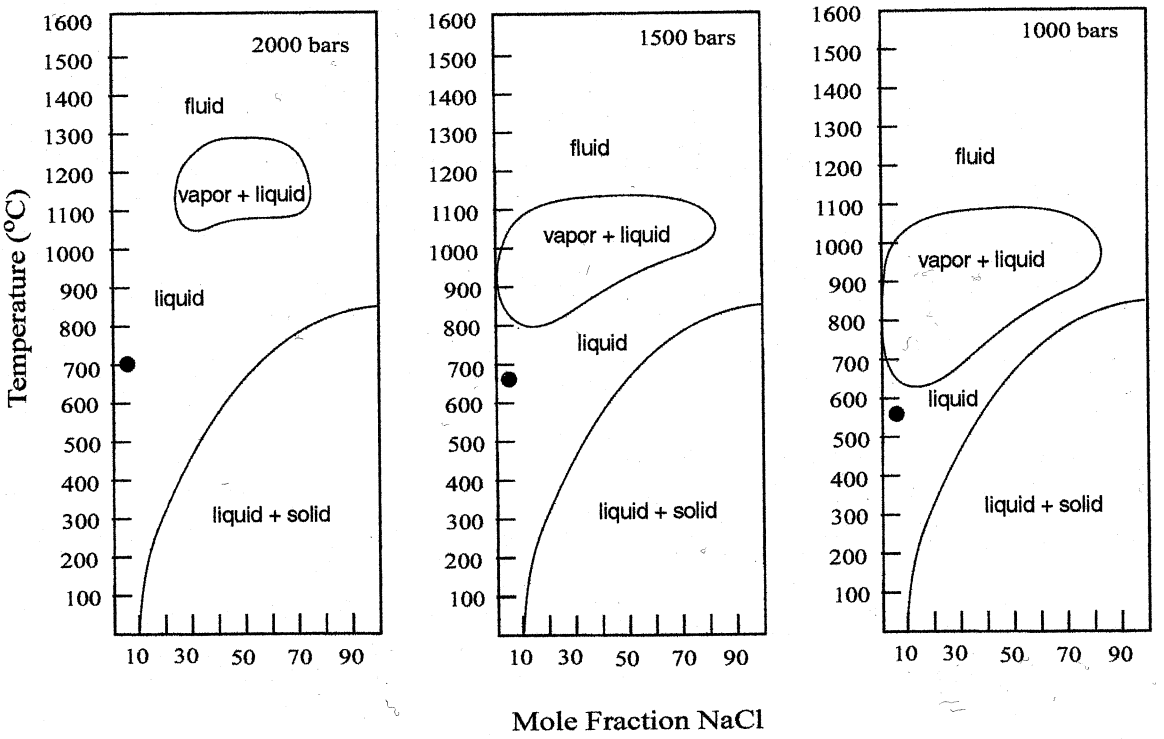
2000 bars
1500 bars
1000 bars
fluid
vapor + liquid
liquid
liquid + solid
Temperature (°C)
Mole Fraction NaCl

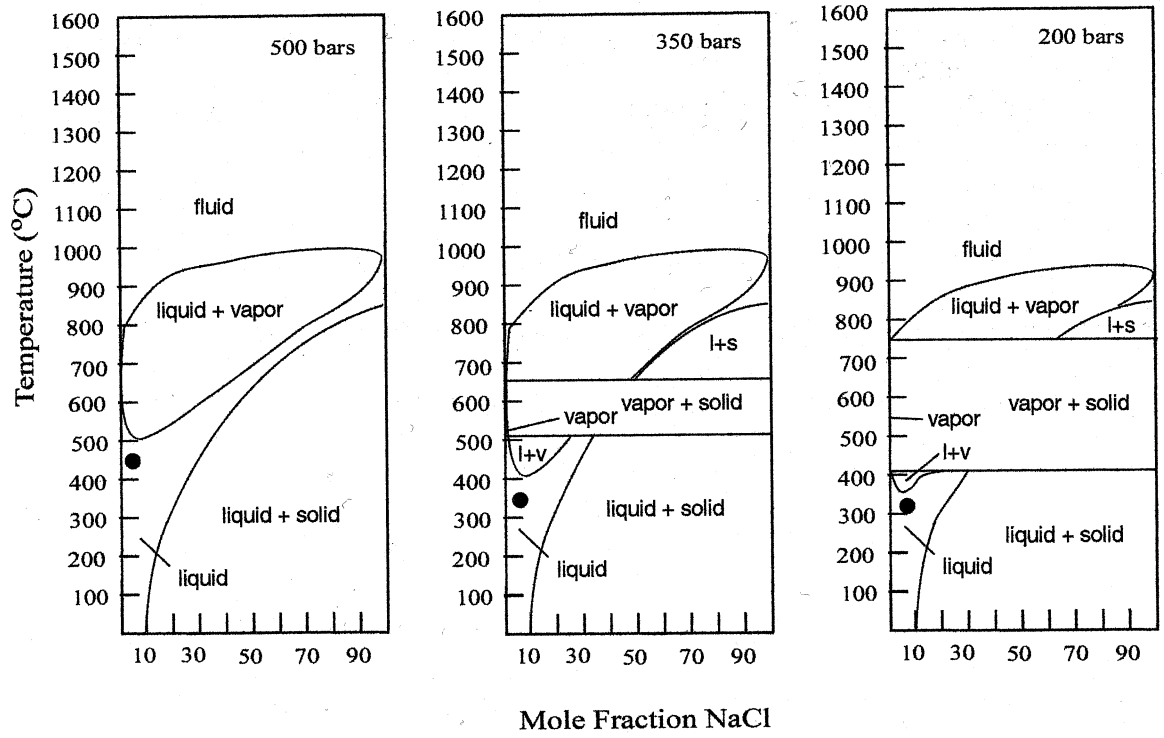
500 bars
350 bars
200 bars
fluid
liquid + vapor
l+s
vapor + solid
vapor
l+v
liquid + solid
liquid
Temperature (°C)
Mole Fraction NaCl

However, as Barnes (1979) points out, at temperatures above 250 °C, solubility of CuCl, the dominant copper-transporting complex in mineralizing fluids, reaches into the thousands of ppm. A solution of 8 eq. wt. % NaCl is therefore more then sufficient to transport the quantity of metals required to form an ore deposit.

As mentioned previously, the homogenization temperature of a fluid inclusion, where there is no evidence of boiling, is simply a minimum estimate of trapping temperature, the entire range of which represented by the calculated pressure-temperature isochores of Figure 16. Extrapolation along these isochores to a pressure of ~350 bars results in a range of trapping temperatures from 375 to 425 °C. The upper end of this temperature range would place the inclusions at the edge of the vapor plus liquid field of Figure 17 (which would likely result in coexisting liquid and vapor dominated inclusions, for which there is no evidence at Tia Maria), effectively constraining the P-T conditions.

Using the diagram for the FeS_2-FeS-Fe_3O_4-H_2S-CO_2-CH_4 system of Norman et al. (1998), as modified by Blamey (2000) to incorporate salinity (Fig. 18), it is possible to estimate the mole % of H_2S that was in equilibrium with pyrite as it was being deposited from the mineralizing fluid. Assuming that the ratio of CO_2/CH_4 is that of a typical magmatic fluid, 10,000 to 1 or more (Giggenbach, 1997), at a temperature of 350 °C and a salinity of 8 eq. wt. % NaCl, H_2S concentration was greater then 0.001 mole %.

Stable Isotopes and Alteration

Most porphyry fluids have a $d^{18}O$ signature that falls between that of traditional magmatic water and the meteoric water line. Values deduced from the K-silicate stable zone that occurs towards the core of a typical porphyry copper deposit are essentially

Figure 18. FeS_2-FeS-Fe_3O_4-H_2S-CO_2-CH_4 system of Norman et al. (1998), as modified by Blamey (2000) to incorporate salinity. Assuming that the ratio of CO_2/CH_4 is that of a typical magmatic fluid, 10,000 to 1 or more (Giggenbach, 1997), at a temperature of 350 ^{o}C and a salinity of 8 eq. wt. % NaCl, H_2S concentration was greater then 0.001 mol %.

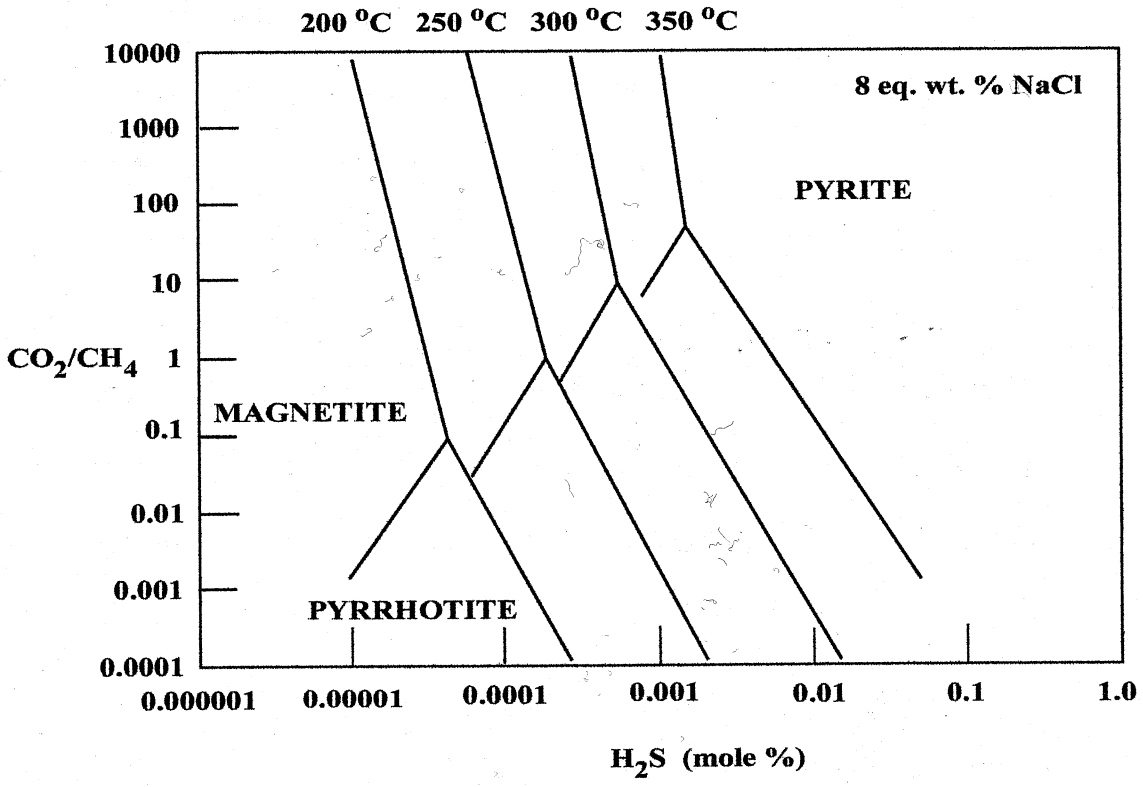
200 °C 250 °C 300 °C 350 °C
8 eq. wt. % NaCl
PYRITE
MAGNETITE
PYRRHOTITE
10000
1000
100
10
1
0.1
0.01
0.001
0.0001
CO2/CH4
0.000001
0.00001
0.0001
0.001
0.01
0.1
1.0
H2S (mole %)

the same as that of the magmatic water box; ~5 to 10 $^{o}/_{oo}$. Further out, in the sericite altered zone, values are O-shifted down to ~0 to 6 $^{o}/_{oo}$, due to mixing with depleted meteoric derived waters (Hedenquist and Lowenstern, 1994).

Using the average primary fluid inclusion homogenization temperature of 360 ^{o}C (see above) and the quartz-H_2O $d^{18}O$ fractionation equation of Matsuhisa et al (1978, 1979), a fractionation of 5.0 $^{o}/_{oo}$ was obtained. This results in an average mineralizing fluid value of 4.0 $^{o}/_{oo}$.

If we recalculate using the upper limit temperature of 425 ^{o}C discussed earlier. the quartz-water fractionation drops to 3.6 $^{o}/_{oo}$, giving an average mineralizing fluid $d^{18}O$ signature of ~5.4 $^{o}/_{oo}$ (Table 3).

$d^{18}O$ of 4.0 to 5.4 $^{o}/_{oo}$ are right at the lower edge of the traditional magmatic water box. Bearing in mind the caveats of the possibly high initial $d^{18}O$ of local meteoric waters and the known enrichment of deeply circulating meteoric waters mentioned in the introduction, it can be stated that regardless of where in the 360 to 425 ^{o}C temperature range the fluid inclusions were actually trapped, it seems most likely that the fluids that mineralized the Tia Maria prospect were of dominantly magmatic origin, with some meteoric component.

The $d^{18}O$ depletion of the altered wall rocks relative to the isotopic signature of more distal, "unaltered" rocks, depends on: 1) the initial isotopic composition of the wall rocks, 2) the composition of the alteration minerals deposited and 3) the isotopic reequilibration between the fluids and the original wall rock minerals. Inferences about the water-rock ratio, on which the third factor greatly depends, can be made from the first two. Less altered, distal host rocks had a $d^{18}O$ of 10.7 to 11.4 $^{o}/_{oo}$, while the more altered host rocks taken from drill core were depleted by only ~1 to 3 $^{o}/_{oo}$, to a $d^{18}O$ of

Table 3
Quartz Water Fractionations

Location	$d^{18}O$ (quartz)	Temp (Th)	1000lna	$d^{18}O$ (water)	Temp (inferred)	1000lna	$d^{18}O$ (water)
	‰	(C)	‰	‰	(C)	‰	‰
Tia Maria							
CAD-003-127	9.0	360	5.0	4.0	425	3.6	5.5
CAD-002-213.4	8.9	360	5.0	3.8	425	3.6	5.3
CAD-002-86.5	9.0	360	5.0	4.0	425	3.6	5.5
CAD-001-108	8.4	360	5.0	3.4	425	3.6	4.9
CAD-001-97.4	9.3	360	5.0	4.3	425	3.6	5.8
CAD-003-263	8.8	360	5.0	3.7	425	3.6	5.2
CAD-002-87.5	9.0	360	5.0	3.9	425	3.6	5.4
CAD-002-194.5	9.2	360	5.0	4.1	425	3.6	5.6
CAD-002-46.9	9.2	360	5.0	4.1	425	3.6	5.6
CAD-001-129.2	9.2	360	5.0	4.1	425	3.6	5.6
Rosa Maria							
West Yanomayo	15.1	250-280	8.9-7.6	6.2-7.5			
Lourdes	13.8	250-280	8.9-7.6	4.9-6.1			
Yanomayo	13.0	250-280	8.9-7.6	4.2-5.4			
Cahuintala	10.2	250-280	8.9-7.6	1.3-2.5			
Rosa Maria	11.0	250-280	8.9-7.6	2.1-3.3			
Saturno	11.1	250-280	8.9-7.6	2.2-3.4			
drill core	11.8	250-280	8.9-7.6	2.9-4.2			

8.5 to 9.5 $^{o}/_{oo}$. Alteration of the host rocks is not pervasive and ranges from 30 to 80 % replacement, with most samples examined being below 50 %. There is no strong correlation between degree of alteration and isotopic depletion in the altered samples. For example, the granodiorite that occurs approximately 110 m down hole in CAD-001 shows about 30 % alteration (Appendix 1) and has a $d^{18}O$ of 8.9 $^{o}/_{oo}$ (Table 2) while at 20 m depth in CAD-002 it is over 60 % altered yet has a $d^{18}O$ of 9.2 $^{o}/_{oo}$. This suggests that the oxygen isotope shift is not controlled by the degree of alteration. The relatively small isotopic shift of the host rocks combined with the generally muted alteration regime, suggests that this system had a low water to rock ratio.

Although the data collected from the Rosa Maria veins was limited, some statements can be made. The lower temperature quartz-H_2O $d^{18}O$ fractionation equation of Matsuhisa et al (1978, 1979) was applied to the Rosa Maria vein results, using the fluid inclusion homogenization temperature range of 250 and 280 °C. For 250 °C, a quartz-H_2O $d^{18}O$ fractionation of 8.9 $^{o}/_{oo}$ was obtained and for 280 °C, 7.6 $^{o}/_{oo}$. Using these values, a range of 1.3 to 7.5 $^{o}/_{oo}$ was obtained for the mineralizing fluids.

While the Tia Maria veins have well grouped $d^{18}O$ values, the Rosa Maria veins vary over a range of more the 5 $^{o}/_{oo}$. Even if this range in the raw data is an artifact of different quartz-water equilibration temperatures, it still implies a significantly larger vertical and horizontal variation then is present in the Tia Maria veins, which display fairly uniform homogenization temperatures throughout.

Conclusions

A Genetic Model

A typical model for a copper porphyry involves the cooling of a hydrous magma stock (Burnham, 1979, 1997). As a magma body cools from the outside in, the outer edge of the stock crystallizes and closes off the rest of the magma to any volatile escape. Beneath this crust is formed a carapace of H_2O saturated interstitial melt. As this cools, a separate H_2O phase separates from the melt (known as resurgent or second boiling) with a concurrent increase in volume. As the crust prevents any expansion, the pressure increases significantly. Eventually the internal pressure exceeds the tensile strength of the roof and overlying rock and the system "bursts", allowing the saline, magmatic H_2O to escape up the fracture system that has been created. As pressure and temperature decreases, the system develops a another crust and the process starts again. Each subsequent time that this process occurs, the crust forms deeper and the amount of water released and the internal pressures reached (due to the reduced tensile strength of the fractured confining rocks) is decreased. This whole process creates multiple generations of overlapping fracture systems and stockworks. A good example of this is the El Salvador copper porphyry in Chile (Gustafsen and Hunt, 1975).

Tia Maria has a fracture system of strictly limited development and only one major generation of stockwork veins. In combination with the relatively small oxygen isotope depletion of the host rocks and the restricted degree of alteration, this suggests a system that is deficient in water.

A lack of water may be explained in several ways. As detailed in the introduction, the intrusive rocks of the southern Coastal Batholith are of largely upper mantle derived origin with a varying, although small, crustal component. These mantle

derived melts tend to be fairly low in water and other volatiles (Pitcher and Cobbing, 1985; Taylor, 1997), and indeed, the intrusions of the Coastal Batholith are commonly described as having dry or water-undersaturated-melt textures (Pitcher, 1984; Mason, 1985) that only rarely concentrated water to the saturation point (Pitcher et al., 1985). As detailed earlier, ore deposits that required abundant volatiles did form from Coastal Batholith intrusives, so there must be an alternate cause of a deficiency of water.

Further evidence comes from the alteration. The poorly developed K-silicate alteration and pervasive propylitic alteration suggests a location somewhat distal to the source intrusive (Reed, 1997). It shows some resemblance to the San Manuel-Kalmazoo (Lowell and Guilbert, 1970) and Los Loros (Sillitoe, 1973) porphyries in their deeper (but not contact metamorphosed/skarnified, intrusive adjacent) levels. The magmatic isotopic signature of the mineralizing fluids and lack of more then incipient quantities of late stage alteration (ie. argillic) suggests that we not located so far from the intrusive as to be in the upper levels of the system, in the convectively circulating meteoric water cell that is thought to develop there (eg. Sillitoe, 1989).

This leaves open the possibility of a deep intrusive. The solubility of water in a melt (and therefore the efficiency of the resurgent boiling process) depends greatly on the pressure. For example, a silicic melt with an initial water content of 2.5 % need only crystallize some 8 % at a pressure of 0.5 kbar to achieve saturation, while the same melt at 2.0 kbar requires at least 59 % crystallization to achieve saturation (Cline 1995). This would also affect the copper in the melt. As copper acts a somewhat compatible element in a melt, the more the melt crystallizes, the less copper will remain in the melt, available for extraction by the exsolving brine (Candela and Holland, 1986).

As a result, a deep intrusive would act much like a shallow porphyry stock undergoing the late stages of the crystallization and fluid escape process, exsolving, quite possibly only in a single pulse, a limited amount of water. There would of course be none of the effects, such as overlapping networks of fractures and stockworks, of multiple cycles (Burnham, 1979).

While the Rosa Maria and Tia Maria veins show significant differences, their spatial superimposition and their similar time of emplacement (~ 160 to 145 Ma; Clark et al., 1990), which is some 50 to 100 Ma older then that of most of the mineralization in the southern Coastal Batholith, is difficult to ignore. The Tia Maria quartz veins have equigranular, anhedral crystals with paragenetically late sulfides. The Rosa Maria veins have bladed quartz with distinctive growth bands, have open spaces and vugs and have a multigenerational paragenesis. Based on the limited data obtained, the Rosa Maria veins have liquid to vapor homogenization temperature approximately 80 to 100 degrees lower temperatures [in the epithermal range, (Hayba et al.,1985)] than the Tia Maria veins, which also display a greater uniformity. The oxygen isotope data also supports the idea of separate events. Unlike the more homogenous Tia Maria veins, the Rosa Maria veins vary over a range of more the 5 $^{o}/_{oo}$. Even if this range in the raw data is an artifact of different quartz-water equilibration temperatures, it still implies a significantly larger amount of lateral and vertical variation in chemical or physical conditions then was present in the Tia Maria veins.

The textural differences, the lower homogenization and the evidence of boiling suggest that the Rosa Maria veins formed at a lower pressure temperature regime. Rosa Maria may be an epithermal type system that formed in the late stages of the formation

Tia Maria, as the porphyry hydrothermal system was collapsing and fracturing had reduced the pressure from lithostatic to hydrostatic.

References

Agar, R.A., 1981. Copper mineralization and magmatic hydrothermal brines in the Rio Pisco section of the Peruvian Coastal Batholith. Economic Geology, v.76, p.677-693

Aguirre, L., Pitcher, W.S. and Cobbing, E.J., 1984. The Geology of the granitoid rocks and their envelope in coastal Peru, Sheet 1 (1:500,000) in, Pitcher, W.S., Atherton, M.P., Cobbing, E.J. and Beckinsale, R.D., eds., 1985. Magmatism at a Plate Edge, the Peruvian Andes, Blackie & Son Ltd., Glasgow.

Albino, G.V., 1995. Porphyry copper deposits of the Great Basin - Nevada, Utah and adjacent California, in, Pierce, F.W. and Bolm, J.G. eds., Porphyry Copper Deposits of the American Cordillera. Arizona Geological Society, Digest no. 20, Tucson.

Anderson, J.,A., 1982. Characteristics of leached capping and techniques of appraisal, in, Titley, S.,R., eds., Advances in Geology of the Porphyry Copper Deposits, Southwestern North America. Tucson, University of Arizona Press.

Anthony, J. W., Bideaux, R. A., Grant, R. W. and Williams, S. A., 1995. Mineralogy of Arizona, University of Arizona Press, Tucson

Atherton, M.P., McCourt, W.J., Sanderson, L.M. and Taylor, W.P., 1979. The geochemical character of the segmented Peruvian Coastal Batholith and associated volcanics, in, Atherton, M.P. and Tarney, J., eds., Origin of Granite Batholiths, Geochemical Evidence, Shiva Publishing Ltd., Orpington, U.K.

Atherton, M.P., 1984. The Coastal Batholith of Peru, in, Harmon, R.S. and Barreiro, B.A., eds., Andean Magmatism, Chemical and Isotopic Constraints, Shiva Publishing Ltd., Nantwick, U.K.

Atherton, M.P. and Sanderson, L.M., 1985. The chemical variation and evolution of the superunits of the segmented Coastal Batholith, in, Pitcher, W.S., Atherton, M.P., Cobbing, E.J. and Beckinsale, R.D., eds., 1985. Magmatism at a Plate Edge, the Peruvian Andes, Blackie & Son Ltd., Glasgow.

Barnes, H.L., 1979. Solubilites of ore minerals, in, in, Barnes, H.L., eds. Geochemistry of Hydrothermal Ore Deposits, 2nd ed., John Wiley and Sons, New York

Barreiro, B.A., 1984. Lead isotope systematics in batholithic rocks of the Western and Coastal Cordilleras, Peru, in, Harmon, R.S. and Barreiro, B.A., eds., Andean Magmatism, Chemical and Isotopic Constraints, Shiva Publishing Ltd., Nantwick, U.K.

Barton, M.D., Staude, J.M.G., Zurcher, L. and Megaw, P.K., 1995. Porphyry copper and other intrusion-related mineralization in Mexico, in, Pierce, F.W. and Bolm, J.G. eds., Porphyry Copper Deposits of the American Cordillera. Arizona Geological Society, Digest no. 20, Tucson.

Beane, R.E. and Bodnar, R.J., 1995. Hydrothermal fluids and hydrothermal alteration in porphyry copper deposits, in, Pierce, F.W. and Bolm, J.G. eds., Porphyry Copper Deposits of the American Cordillera. Arizona Geological Society, Digest no. 20, Tucson.

Bellido, E. and Guevara, C. 1961. Mapa geologico del cuadrangulo de Punto de Bombon (1:100 000), version digital 1998. Lima, Peru, Com. Carta. Geol. Nac.

Benavides, G. and Espinoza, R.L. eds. 1998. Atlas of Mining and Energy in Peru. Lima, Peru, Ministry of Energy and Mines.

Biswas, A.K. and Davenport, W.G., 1994, Extractive metallurgy of copper, 3rd ed., Pergamon, Great Britain.

Blamey, N.J.F., 2000. The evolution of hydrothermal fluids at the Pipeline Gold Mine, Lander County, Nevada. Unpublished Ph.D. dissertation, Socorro, New Mexico: New Mexico Institute of Mining and Geology, 200 p.

Bodnar, R.J., 1995. Fluid-inclusion evidence for a magmatic source of metals in porphyry copper deposits, in, Thompson, J.F.H., eds., Mineralogical Association of Canada Short Course Series v.23, Magmas, Fluids and Ore Deposits, Mineralogical Association of Canada, Victoria, Canada.

Boily, M., Brooks, C., Ludden, J.N. and James, D.E., 1989. Chemical and isotopic evolution of the coastal batholith of southern Peru. Journal of Geophysical Research, v.94, p.12,483-12,498

Borthwick, J., and Harmon, R. S., 1982. A note regarding ClF_3 as an alternative to BrF_5 for oxygen isotope isotope analysis: Geochimica et Cosmochimica Acta, v.74, p.1390-1393

Brown, P. E., 1989. FLINCOR, A microcomputer program for the reduction and investigation of fluid inclusion data: American Mineralogist, v.74, p.1390-1393

Burnham, C.W., 1979. Magmas and hydrothermal fluids, in, Barnes, H.L., eds. Geochemistry of Hydrothermal Ore Deposits, 2nd ed., John Wiley and Sons, New York

Burnham, C.W., 1997. Magmas and hydrothermal fluids, in, Barnes, H.L., eds. Geochemistry of Hydrothermal Ore Deposits, 3rd ed., John Wiley and Sons, New York

Campbell,A.R. and Larsen, P.B. 1998. Introduction to stable isotope applications in hydrothermal systems, in, Richards, J.P. and Larsen, P.B., eds., Techniques in Hydrothermal Ore Deposit Geology: Reviews in Economic Geology, v.10, Society of Economic Geologists, p.173-192

Candela, P.A., and Holland, H.D., 1986. A mass transfer model for copper and molybdenum in magmatic hydrothermal systems: the origin of porphyry-type ore deposits. Economic Geology, v.81, p.1-19

Carten, R.B., 1986. Sodium-calcium metasomatism: Chemical, temporal, and spatial relationships at the Yerington, Nevada, porphyry copper deposit. Economic Geology, v.81, p.1495-1519

Chavez Jr., W.X., 2000. Supergene oxidation of copper deposits: zoning and distribution of copper oxide minerals. Society of Economic Geologists Newsletter. n.41, p.1-19

Clark, A.H., Farrar, E., Kontak, D.J., Langridge, R.J., Arenas F., M.J., France, L.J., Mcbride, S.L., Woodman, P.L., Wasteneys, H.A., Sandeman, H.A. and Archibald, D.A., 1990a. Geologic and geochronologic constraints of the metallogenic evolution of the Andes of southeastern Peru. Economic Geology. v.85, p.1520-1583

Clark, A.H., Tosdal, R.M., Farrar, E. and Plazolles V., A., 1990b. Geomorphologic environment and age of supergene enrichment of the Cuajone, Quellaveco and Toquepala porphyry copper deposits, southeastern Peru. Economic Geology. v.85, p.1604-1628

Clayton, R. N., and Mayeda, T. K., 1963. The use of bromine pentafluoride in the extraction of oxygen from oxides and silicates for isotopic analysis. Geochimica et Cosmochimica Acta, v.27, p.43-52

Cline, J.S., 1995. Genesis of porphyry copper deposits: The behavior of water, chloride, and copper in crystallizing melts, in, Pierce, F.W. and Bolm, J.G. eds., Porphyry Copper Deposits of the American Cordillera. Arizona Geological Society, Digest no. 20, Tucson.

Cobbing, E.J. and Moore, N.D., 1984. The Geology of the granitoid rocks and their envelope in coastal Peru, Sheet 2 (1:500,000) in, Pitcher, W.S., Atherton, M.P., Cobbing, E.J. and Beckinsale, R.D., eds., 1985. Magmatism at a Plate Edge, the Peruvian Andes, Blackie & Son Ltd., Glasgow.

Cobbing, E.J., 1985. The tectonic setting of the Peruvian Andes, in, Pitcher, W.S., Atherton, M.P., Cobbing, E.J. and Beckinsale, R.D., eds., Magmatism at a Plate Edge, the Peruvian Andes, Blackie & Son Ltd., Glasgow.

Dilles, J.H., and Einaudi, M.T., 1992. Wall-rock alteration and hydrothermal flow paths about the Ann-Mason porphyry copper deposit, Nevada - a 6-km vertical reconstruction. Economic Geology, v.87, p.1963-2001

Eastoe, C.J., 1978. A fluid inclusion study of the Panguna porphyry copper deposit, Bouganville, Papua New Guinea. Economic Geology, v.73, p.721-748

Field, C.W. and Fifarek, R.H., 1985. Light stable-isotope systematics in the epithermal environment. in, Berger, B.R. and Bethke, P.M., eds., Geology and Geochemistry of Epithermal Systems: Reviews in Economic Geology, v.2, Society of Economic Geologists p.99-128

Foord, E. E., Gaines, R. V., King, V. T., Mason, B., Rosenzweig, A. and Skinner, H.C.W., 1997. Dana's New Mineralogy. John Wiley and Sons, Inc. New York.

Fuller, A.O., 1979. Phosphate occurrences on the western and southern coastal areas and continental shelves of southern Africa. Economic Geology. v.74, p.221-231

Garcia, W. and Landa, C., 1968. Mapa geologico del cuadrangulo de la Joya. (1:100 000). Lima, Peru, Com. Carta. Geol. Nac.

Gendall, I.R., Quevedo, L.A., Sillitoe, R.H., Spencer, R.M., Puente, C.O., Leon, J.P. and Povedo, R.R., 2000. Discovery of a Jurassic porphyry copper belt, Pangui area, southern Ecuador. Society of Economic Geologists Newsletter. n.43, p.1-15

Giggenbach, W.F., 1997. The origin and evolution of fluids in magmatic-hydrothermal systems, in, Barnes, H.L., eds., Geochemistry of Hydrothermal Ore Deposits, 3rd ed., John Wiley and Sons, Inc, New York

Guilbert, J.M. and Park, C.F., 1986. Ore Deposits. W.H. Freeman and Co. New York.

Gustafson, L.B., and Hunt, J.P., 1975. The porphyry copper deposit at El Salvador, Chile. Economic Geology, v.70, p.857-912

Hayba, D.O., Bethke, P.M., Heald, P., and Foley, N.K., 1985. Geologic, mineralogic, and geochemical characteristics of volcanic hosted epithermal precious-metal deposits ,in, Berger, B.R. and Bethke, P.M., eds., Geology and Geochemistry of Epithermal Systems: Reviews in Economic Geology, v.2, Society of Economic Geologists p.99-128

Hedenquist, J.W. and Lowenstern, J.B., 1994. The role of magmas in the formation of hydrothermal ore deposits. Nature, v. 370, p.519-527

Hedenquist, J.W, Arribas, A. and Reynolds, T.J., 1998. Evolution of an intrusion -centered hydrothermal system: Far Southest-Lepanto porphyry and epithermal Cu-Au deposits, Philippines. Economic Geology, v.93, p.373-404

Henley, R.W. and McNabb, A., 1978. Magmatic vapor plumes and ground-water interaction in porphyry copper emplacement. Economic Geology. v.73, p.1-20

Hoefs, J., 1997. Stable Isotope Geochemistry, 4th ed. Springer-Verlag. Berlin, Germany.

Jaillard, E. and Soler, P., 1996. Cretaceous to early Paleogene tectonic evolution of the northern Central Andes (0-18°S) and its relations to geodynamics. Tectonophysics, v.259, p.41-53

Keith, S.B. and Swan, M.M., 1995. Tectonic setting, petrology, and genesis of the Laramide porphyry copper cluster of Arizona, Sonora and New Mexico, in, Pierce, F.W. and Bolm, J.G. eds., Porphyry Copper Deposits of the American Cordillera. Arizona Geological Society, Digest no. 20, Tucson.

LeMaitre, R.W., 1989. A classification of igneous rocks and glossary of terms. in, Recommendations of the International Union of Geological Sciences Subcommsion of the Systematics of Igneous Rocks. Blackwell Scientific Publications, London.

Locke, A., 1926. Leached Outcrops as a Guide to Copper Ores. Baltimore, Williams and Wilkins Co.

Lowell J.D. and Guilbert, J.M., 1970. Lateral and vertical alteration-mineralozation zoning in porphyry ore deposits. Economic Geology, v.65, p.373-408

Magalhaes, M.C.F., Pedrosa de Jesus, J. and Williams, P.A., 1986. Stability constants and formation of Cu(II) and Zn(II) phosphate minerals in the oxidized zone of base metal orebodies. Mineralogical Magazine. v.50, p.41-47

Mason, G.H., 1985. The mineralogy of the Coastal Batholith of Peru, in, Pitcher, W.S., Atherton, M.P., Cobbing, E.J. and Beckinsale, R.D., eds. Magmatism at a Plate Edge, the Peruvian Andes, Blackie & Son Ltd., Glasgow.

Matsuhisa, Y., Goldsmith, J.R. and Clayton, R.N., 1978. Mechanisms of hydrothermal crystallization of quartz at 250 °C and 15 kbar. Geochimica et Cosmochimica Acta, v.42, p.173-182

___ 1979. Oxygen isotope fractionation in the system quartz-albite-anorthite-water. Geochimica et Cosmochimica Acta, v.43, p.1131-1140

Megard, F., 1987. Structure and evolution of the Peruvian Andes, in, Schaer, J.P. and Rodgers, J., eds., The Anatomy of Mountain Ranges, Princeton University Press, Princeton, New Jersey.

Melchiorre, E.B., Criss, R.E. and Rose, T. P., 1999. Oxygen and carbon isotope study of natural and synthetic malachite. Economic Geology, v.94, p.245-260

___ 2000. Oxygen and carbon isotope study of natural and synthetic azurite. Economic Geology, v.95, p.621-628

Murr, L.E., 1980, Theory and practice of copper sulfide leaching in and *in situ* , Minerals Science and Engineering, v. 12, p. 121-189.

Musaka, S.B. and Tilton, G.R., 1984. Lead isotope systematics in batholithic rocks of the Western and Coastal Cordilleras, Peru, in, Harmon, R.S. and Barreiro, B.A., eds., Andean Magmatism, Chemical and Isotopic Constraints, Shiva Publishing Ltd., Nantwick, U.K.

Nesbitt, B. and Muenhlenbachs, K., 1995. Geochemical studies of the origins and effects of synorogenic crustal fluids in the southern Omineca Belt of British Columbia, Canada. Geological Society of America Bulletin, v.107, p.1033-1050

Newberg, D.W., 1967. Geochemical implications of chrysocolla-bearing alluvial gravels. Economic Geology, v.62, p.932-956

Norman, D.I., Chomiak, B.A., and Moore, J.N., 1998. Approaching equilibrium from the hot and cold sides in the FeS_2-FeS-Fe_3O_4-H_2S-CO_2-CH_4 system in the light of fluid inclusion gas analysis, in, Arehart, G.B., and Hulston, J.R., eds., Proceedings of the 9th International Symposium on Water-Rock Interaction: Rotterdam, A.A. Balkema, p565-568.

Phelps Dodge, 2000. Geologia de los Porfidos de Cobre Cerro Verde y Santa Rosa. Departamento de Geologia, Arequipa, Peru.

Pinson, P., 1992. Quantitative supergene mineralogic study of a porphyry copper system in the southwestern United States. Unpublished M.S. thesis, Socorro, New Mexico: New Mexico Institute of Mining and Technology, 140 p.

Pitcher, W.S., 1984. Phanerozoic plutonism in the Peruvian Andes, in, Harmon, R.S. and Barreiro, B.A., eds., Andean Magmatism, Chemical and Isotopic Constraints, Shiva Publishing Ltd., Nantwick, U.K.

Pitcher, W.S., Atherton, M.P., Cobbing, E.J. and Beckinsale, R.D., 1985. A model for the Coastal Batholith, in, Pitcher, W.S., Atherton, M.P., Cobbing, E.J. and Beckinsale, R.D., eds. Magmatism at a Plate Edge, the Peruvian Andes, Blackie & Son Ltd., Glasgow.

Pitcher, W.S. and Cobbing, E.J., 1985. Epilogue, in, Pitcher, W.S., Atherton, M.P., Cobbing, E.J. and Beckinsale, R.D., eds. Magmatism at a Plate Edge, the Peruvian Andes, Blackie & Son Ltd., Glasgow.

Richards, J.P., Noble, S.R. and Pringle, M.S., 1999. A revised late Eocene age for porphyry Cu magmatism in the Escondida area, northern Chile. Economic Geology, v.94, p.1231-1248

Roedder, E., 1984. Fluid Inclusions. Reviews in Mineralogy, v.12. Mineralogical Society of America, Reston, Virginia.

Roedder, E. and Bodnar, R.J., 1997. Fluid inclusion studies of hydrothermal ore deposits, in, Barnes, H.L., eds., Geochemistry of Hydrothermal Ore Deposits, 3rd ed., John Wiley and Sons, Inc, New York

Reed, M.H., 1997. Hydrothermal alteration and its relationship to ore fluid composition, in, Barnes, H.L., eds., Geochemistry of Hydrothermal Ore Deposits, 3rd ed., John Wiley and Sons, Inc, New York

Rose, A.W. and Burt, D.M., 1979. Hydrothermal alteration, in, Barnes, H.L., eds. Geochemistry of Hydrothermal Ore Deposits, 2nd ed., John Wiley and Sons, New York

Sato, M., 1960. Oxidation of sulfide ore bodies: 1, geochemical environments in terms of Eh and pH. Economic Geology, v.55, p.928-961

Shakleton, R.M., Ries, A.C., Coward, M.P. and Cobbold, P.R., 1979. Structure, metamorphism and geochronology of the Arequipa massif of coastal Peru. Geological Society of London Journal, v.136, p.195-214

Sheets, R.W., Nesbitt, B.E. and Muehlenbachs, K. 1996. Meteoric water component in magmatic fluids from porphyry copper mineralization, Babine Lake area, British Columbia. Geology, v.24, p.1091-1094

Sillitoe, R.H., 1973. The tops and bottoms of porphyry copper deposits. Economic Geology, v.68, p.799-815

Sillitoe, R.H., 1977. Permo-Carboniferous, Upper Cretaceous, and Miocene porphyry copper-type mineralization on the Argentinian Andes. Economic Geology, v.72, p.99-103

Sillitoe, R.H., Jaramillo, L., Damon, P.E., Shafiquillah, M. and Escovar, R., 1982. Setting, characteristics, and age of the Andean porphyry copper belt in Colombia. Economic Geology, v.77, p.1837-1850

Sillitoe, R.H., 1989. Gold deposits in western Pacific island arcs: the magmatic connection. Economic Geology, v.84, p.274-291

Taylor, H.P., 1997. Oxygen and hydrogen isotope relationships in hydrothermal mineral deposits, in, Barnes, H.L., eds., Geochemistry of Hydrothermal Ore Deposits, John Wiley and Sons, New York.

Titley, S.R. and Chavez Jr., W.X., 1999. Field and mine mapping short course. Society of Economic Geologists, University of Arizona, Tucson.

Titley, S.R. and Marozas, D.C., 1995. Processes and products of supergene copper enrichment, in, Pierce, F.W. and Bolm, J.G. eds., Porphyry Copper Deposits of the American Cordillera. Arizona Geological Society, Digest no. 20, Tucson.

Vidal, C.E., 1985. Metallogenesis associated with the Coastal Batholith of Peru: a review, in, Pitcher, W.S., Atherton, M.P., Cobbing, E.J. and Beckinsale, R.D., eds., 1985. Magmatism at a Plate Edge, the Peruvian Andes, Blackie & Son Ltd., Glasgow.

Vink, B.W., 1986. Stability relations of malachite and azurite. Mineralogical Magazine. v.50, p.41-47

Williams, S.A. and Forrester, J.D., 1995. Characteristics of porphyry copper deposits, in, Pierce, F.W. and Bolm, J.G. eds., Porphyry Copper Deposits of the American Cordillera. Arizona Geological Society, Digest no. 20, Tucson.

Appendix 1

Petrographic Descriptions

All petrographic descriptions made from standard thickness (30mm) thin sections without cover slips. Rock names are based on standard IUGS ternary diagrams (see Fig. 6). Listed mineralogy is the interpreted magmatic original while written description is what is currently observed.

Sample ID: CAD-001 32.0m
Rock Name: Hornblende Monzogranite
Texture: equigranular, 0.1 to 1.0mm

Mineral	Percentage	Notes
Quartz	50 %	Occurs as aggregates of grains with undulatory extinction.
Plagioclase	15 %	
K-feldspar	20 %	
Hornblende	10 %	Nearly 100 % altered.
Biotite	5 %	Occurs as small patches and stringers.
Magnetite	minor	Irregular grains associated with biotite.

This sample displays several styles of alteration. Chlorite and rutile largely replace the paragenetically late biotite. This alteration is overprinted by white phyllosilicate ("sericite") alteration. Plagioclase displays ~ 15 % replacement by sericite and K-feldspar shows ~ 10 % while the chlorite after biotite shows only minor alteration. What are interpreted as former hornblende phenocrysts are essentially totally replaced by sericite $\pm$ magnetite. This magnetite differs from the magmatic magnetite by being smaller, more euhedral and by its association with patches of very strong sericite alteration. Traces of kaolinite also occur associated with the sericite.

Sample ID: CAD-001 108.0m
Rock Name: Granodiorite
Texture: equigranular, 0.1 to 1.0mm

Mineral	Percentage	Notes
Quartz	45 %	Occurs as aggregates of grains with undulatory extinction.
Plagioclase	35 %	
K-feldspar	10 %	
Mafics	10 %	Totally replaced by chlorite and rutile $\pm$ magnetite

This sample displays similar alteration to the above sample. What are interpreted as former biotites and hornblendes are replaced entirely by chlorite and rutile with the rare relict biotite appearing in the replacing chlorite. Traces of magnetite occur with the chlorite where hornblende has been replaced. Chlorite also occurs as a scattered interstitial phase, probably replacing minor groundmass. The chlorite alteration is slightly overprinted by sericite alteration. Plagioclase is heavily replaced (as much as 80 %) by sericite while K-feldspar shows up to 30 % replacement.

Sample ID: CAD-001 180.25m
Rock Name: Biotite Monzogranite
Texture: equigranular, 0.1 to 1.0mm

Mineral	Percentage	Notes
Quartz	50 %	Fewer agglomerates of smaller grains with undulatory extinction then the above samples
Plagioclase	20 %	
K-feldspar	20 %	
Mafics	10 %	Totally replaced by chlorite and rutile

As with the previous sample, biotite and hornblende are completely replaced by chlorite and rutile with occasional relicts of the original mineral surviving. However, magnetite does not occur as an alteration product with the chlorite. Chlorite also occurs as a scattered interstitial phase, probably replacing minor groundmass. The chlorite alteration displays some overprint by sericite alteration, especially adjacent to rutile grains. Plagioclase is replaced up to 50 % by sericite while K-feldspar shows much less well developed alteration (not more then 10 % replacement). The amorphous hydrous copper silicate mineraloid chrysocolla fills voids and possibly replaces mafic minerals adjacent to those voids.

Sample ID: CAD-001 206.4m
Rock Name: Biotite Monzogranite
Texture: equigranular, 0.1 to 1.0mm

Mineral	Percentage	Notes
Quartz	50 %	Occurs in grains that are equigranular with feldspars. Occasional undulatory extinction
Plagioclase	20 %	
K-feldspar	20 %	
Biotite (primary)	10 %	Magmatic biotite ~80 % replaced by secondary biotite

In hand specimen, this sample displays an incipient Schlarin texture. However, in thin section, the biotite that defines this "proto-banding" does not display preferred orientation or evidence of deformation. The crude "bands" of homogeneous magmatic biotite in this sample are ~ 80 % replaced by a lighter, shreddy biotite that also occurs interstitially. The secondary biotite, especially in the interstitial variety, displays some chlorite and rutile replacement along with rare opaque iron oxides. Plagioclase is up to 30 % replaced by sericite while K-feldspar shows up to 30 % replacement. Quartz in this sample also occurs as crosscutting stringers of small grains displaying undulatory extinction. This is interpreted as silicification accompanying phyllic alteration.

Sample ID: CAD-001 225.4.0m
Rock Name: Hornblende Granodiorite
Texture: equigranular, 0.1 to 1.0mm

Mineral	Percentage	Notes
Quartz	40 %	Predominantly equigranular grains with occasional veinlets composed of small, irregular grains
Plagioclase	30 %	
K-feldspar	20 %	Also occurs as rare, tiny, late veinlets
Hornblende	10 %	Totally replaced by biotite $\pm$ quartz

The "proto-banding" shown by the previous sample is not in evidence in CAD-001 225.4m. What is interpreted as former biotite is totally replaced by coarse and blocky secondary biotite with minor quartz occurring between the blades. The biotite shows traces of alteration by chlorite $\pm$ epidote. Chlorite also occurs as tiny veinlets that

crosscut feldspar phenocrysts. Both feldspars show patchy alteration by sericite. The intensity of this varies from almost none up to 50 %.

Sample ID: CAD 002 14.2m
Rock Name: Andesite Porphyry
Texture: porphyritic; groundmass, 0.1 to 0.5mm
phenocrysts, 1.0 to 2.0mm

Mineral	Percentage	Notes
Feldspar	30	Phenocrysts; Total alteration prevents specific identification
Feldspar	45	Groundmass; as above
Quartz	20	Groundmass
Mafics	5	100% replaced by chlorite $\pm$ magnetite

This sample has been heavily altered. The feldspar phenocrysts and groundmass are 100% replaced and are therefore not more specifically identifiable. Alteration is sericite with an incipient argillic overprint visible interstitially in the groundmass and at the edges of the phenocrysts. What are interpreted as former hornblende phenocrysts are essentially totally replaced by chlorite $\pm$ magnetite with a slight sericite overprint. Patches and veinlets of quartz with undulatory extinction cut the sample. The quartz ranges in size from that of groundmass up to 2mm. Slightly more argillic alteration appears in the groundmass along the boundaries of the quartz crystals then elsewhere.

Sample ID: CAD-002 23.4m

Rock Name: Granite to Granodiorite
Texture: Equigranular, 0.1 to 1.0mm

Mineral	Percentage	Notes
Quartz	40 %	Occurs as patchy, granular masses
Plagioclase	~ 25 %	Too altered by sericite and kaolinite to determine exact proportions
K-feldspar	~ 25 %	
Mafics	~ 10 %	Totally replaced by sericite $\pm$ rutile

This sample is very heavily altered. Plagioclase is replaced up to 80 % by sericite while K-feldspar shows about 50 % replacement. Kaolinite occurs with the sericite, especially along cleavages in the plagioclase. Blades of sericite occur along quartz grain boundaries and fractures. Mafic minerals are totally obliterated by sericite with

relict rutile grains remaining. The rutile grains may be the result of phyllic alteration overprinting the chlorite + rutile alteration of biotite and hornblende.

Sample ID: CAD 003 48.8m
Rock Name: Tonalite Porphyry
Texture: porphyritic; groundmass, 0.1 to 0.5mm
phenocrysts, 1.0 to 2.0mm

Mineral	Percentage	Notes
Plagioclase	35	Phenocrysts; 90% alteration
Plagioclase	30	Groundmass; near total alteration
Quartz	25	Groundmass
Mafics	10	100% replaced by chlorite $\pm$ magnetite

The plagioclase phenocrysts in this sample display almost total replacement by sericite, although enough remains for identification. The groundmass plagioclase is almost totally altered by sericite slightly overprinted by argillic alteration. What are interpreted as former hornblendes are completely replaced by completely $\pm$ magnetite. This sample is cut by fine quartz veinlets displaying undulatory extinction.

Sample ID: CAD 003 190.8m
Rock Name: Hornblende Granodiorite Porphyry
Texture: porphyritic; groundmass, 0.1 to 0.5mm
phenocrysts, 1.0 to 2.0mm

Mineral	Percentage	Notes
Plagioclase	50	Phenocrysts; very highly variable degree of alteration
Quartz	15	Phenocrysts
Feldspar	15	Groundmass; 100% replaced
Quartz	10	Groundmass
Mafics	10	100% replaced by chlorite $\pm$ magnetite

This sample displays a highly variable degree of replacement. The plagioclase phenocrysts display alteration by sericite $\pm$ kaolinite which increases from 10% on one edge of the slide to 80% on the other. This may be related to the quartz veinlet that runs along the edge of the slide that shows the most replacement. However, this relationship may be coincidental since this alteration gradient is not observed in relation to quartz veinlets in other samples. The feldspar in the groundmass is altered beyond recognition to sericite with a slight argillic overprint. What are interpreted as former

hornblende phenocrysts are essentially totally replaced by chlorite ± magnetite. Interstitial mafics are completely replaced by chlorite ± rutile, which suggests that they were originally biotite.

Sample ID: 0203481-8118741
Rock Name: Biotite Quartz-Monzonite Porphyry
Texture: porphyritic; groundmass, 0.1 to 0.5mm
phenocrysts, 1.0 to 2.0mm

Mineral	Percentage	Notes
Plagioclase	50	Phenocrysts; 10% alteration to biotite
K-feldspar	30	Groundmass; up to 50% replaced by sericite
Quartz	15	Groundmass
Biotite	5	>80% replaced by chlorite + rutile ±epidote ± magnetite

Plagioclase phenocrysts display ~ 10 % replacement by sericite while the K-feldspar in the groundmass shows ~ 10 %. There is a well developed granophyric texture where the plagioclase phenocrysts contact the groundmass. while the chlorite after biotite shows only minor alteration. Primary, euhedral biotite phenocrysts are replaced by chlorite + rutile ± epidote. Smaller biotites interstitial to the groundmass are similarly replaced except that magnetite also occurs. As magnetite is not always associated with a chloritized biotite, it may, at least in part, be primary.

Sample ID: 0204685-8118299
Rock Name: Hornblende Biotite Diorite
Texture: porphyritic; groundmass, ~0.1mm
phenocrysts, ~0.5mm

Mineral	Percentage	Notes
Plagioclase	60	Phenocrysts; 10% alteration by sericite
Hornblende	15	Near total replacement by chlorite and secondary biotite
Biotite	15	>60% replacement by chlorite and secondary biotite
Quartz	5	Groundmass
K-feldspar	5	Groundmass; 10% alteration to sericite

Plagioclase occurs predominantly as 0.5mm laths that are ~ 10 % replaced by sericite and rarely as larger, anhedral, phenocrysts displaying up to 30 % alteration. Hornblende phenocrysts are almost totally replaced by chlorite ± rutile ± magnetite

which also overprints patches of shreddy secondary biotite. Biotite is at least 60% replaced by secondary biotite and chlorite ± rutile ± epidote. The K-feldspar in the groundmass shows minor alteration by sericite.

Sample ID: 02033370-8118975
Rock Name: Banded Hornblende Granite
Texture: Equigranular, 0.1 to 1.0mm

Mineral	Percentage	Notes
Quartz	50	
Plagioclase	20	~50% replaced by sericite
K-feldspar	20	~80% replaced by sericite
Hornblende	10	total replacement by chlorite ± magnetite
Biotite	~1	>90% replaced by chlorite ± rutile ± epidote

A crude schlarin texture is evident in this sample in hand specimen. However, in thin section, although there is some segregation of the mafic minerals, there is no preferred orientation of the platy minerals or evidence of deformation. The crude "bands" of hornblende in this sample are almost totally replaced by chlorite ± magnetite ± rutile. The interstitial biotite, which is segregated like the hornblende, is replaced by chlorite with rutile and epidote along with some shreddy secondary biotite. Plagioclase is up to 50 % replaced by sericite while K-feldspar shows as much as 80 % replacement. Quartz in this sample is equigranular with the feldspars.

Appendix 2
Electron Microprobe Analysis of Mineralization
n/d - not detected
n/a -not applicable

Sample	SiO_2	CuO	Al_2O_3	P_2O_5	Fe_2O_3	MnO_2	Identification	CuO/SiO_2
CAD-1-26.0	46.41	36.31	1.42	n/d	n/d	n/d	Chrys	0.78
CAD-1-26.0	31.94	23.66	n/d	n/d	n/d	n/d	Chrys	0.74
CAD-1-26.0	23.41	15.72	n/d	n/d	n/d	n/d	Chrys	0.67
CAD-1-26.0	46.33	35.64	1.40	n/d	n/d	n/d	Chrys	0.77
CAD-1-26.0	44.02	32.38	1.32	n/d	n/d	n/d	Chrys	0.74
CAD-1-26.0	49.07	38.98	1.51	n/d	n/d	n/d	Chrys	0.79
CAD-1-26.0	47.94	37.90	1.47	n/d	n/d	n/d	Chrys	0.79
CAD-1-26.0	43.57	35.70	1.38	n/d	n/d	n/d	Chrys	0.82
CAD-1-26.0	45.97	34.99	1.40	n/d	n/d	n/d	Chrys	0.76
CAD-1-26.0	49.53	41.48	1.28	n/d	n/d	n/d	Chrys	0.84
CAD-1-26.0	49.26	39.88	1.36	n/d	n/d	n/d	Chrys	0.81

Sample	SiO_2	CuO	Al_2O_3	P_2O_5	Fe_2O_3	MnO_2	Identification	CuO/SiO_2
CAD-1-74.7	46.49	50.58	n/d	n/d	n/d	n/d	Chrys	1.09
CAD-1-74.7	48.90	49.68	n/d	n/d	n/d	n/d	Chrys	1.02
CAD-1-74.7	44.09	46.75	n/d	n/d	n/d	n/d	Chrys	1.06
CAD-1-74.7	46.69	49.07	n/d	n/d	n/d	n/d	Chrys	1.05

Sample	SiO_2	CuO	Al_2O_3	P_2O_5	Fe_2O_3	MnO_2	Identification	CuO/SiO_2

CARC-042	25.96	18.02	1.49	n/d	n/d	n/d	Al-Chrys	0.69
CARC-042	45.81	41.08	1.51	n/d	n/d	n/d	Al-Chrys	0.90
CARC-042	46.46	40.95	1.50	n/d	n/d	n/d	Al-Chrys	0.88
CARC-042	25.54	17.95	1.10	n/d	n/d	n/d	Al-Chrys	0.70
CARC-042	45.29	36.11	n/d	n/d	n/d	n/d	Chrys	0.80

Sample	SiO_2	CuO	Al_2O_3	P_2O_5	Fe_2O_3	MnO_2	Identification	CuO/SiO_2
CAD-001-50.4	n/d	66.52	n/d	12.17	n/d	n/d	Psu-Mal	n/a
CAD-001-50.4	13.97	30.48	n/d	n/d	1.20	37.03	Neotocite	2.18
CAD-001-50.4	47.92	50.78	n/d	n/d	n/d	n/d	Chrys	1.06
CAD-001-50.4	25.74	34.94	n/d	n/d	1.58	24.03	Neotocite	1.36
CAD-001-50.4	n/d	66.52	n/d	12.20	n/d	n/d	Psu-Mal	n/a
CAD-001-50.4	99.58	n/d	n/d	n/d	n/d	n/d	Qtz	n/a
CAD-001-50.4	48.23	51.82	n/d	n/d	n/d	n/d	Chrys	1.07
CAD-001-50.4	29.72	36.40	n/d	n/d	5.93	10.60	Neotocite	1.22
CAD-001-50.4	30.61	36.79	n/d	n/d	7.77	8.36	Neotocite	1.20
CAD-001-50.4	22.26	34.11	n/d	n/d	n/d	25.93	Neotocite	1.53
CAD-001-50.4	n/d	64.66	n/d	12.31	n/d	n/d	Psu-Mal	n/a
CAD-001-50.4	n/d	65.33	n/d	12.21	n/d	n/d	Psu-Mal	n/a

Sample	SiO_2	CuO	Al_2O_3	P_2O_5	Fe_2O_3	MnO_2	Identification	CuO/SiO_2
CAD-001-13.0	50.92	10.89	4.04	n/d	3.21	n/d	Cu/Fe Silicate	0.21

CAD-001-13.0	57.69	7.95	4.52	n/d	2.85	n/d	Cu/Fe Silicate	0.14
CAD-001-13.0	56.48	7.89	4.51	n/d	2.86	n/d	Cu/Fe Silicate	0.14
CAD-001-13.0	54.72	6.39	4.47	n/d	2.55	n/d	Cu/Fe Silicate	0.12

Sample	SiO_2	CuO	Al_2O_3	P_2O_5	Fe_2O_3	MnO_2	Identification	CuO/SiO_2
CAD-001-85.4	2.52	1.82	n/d	n/d	38.17	n/d	Goethite	n/a
CAD-001-85.4	100.63	n/d	n/d	n/d	n/d	n/d	Qtz	n/a
CAD-001-85.4	3.50	2.37	n/d	n/d	37.90	2.24	Goethite	n/a
CAD-001-85.4	100.75	n/d	n/d	n/d	n/d	n/d	Qtz	n/a
CAD-001-85.4	88.83	n/d	n/d	n/d	n/d	n/d	Qtz	n/a
CAD-001-85.4	2.83	2.31	n/d	n/d	37.75	1.16	Goethite	n/a

Sample	SiO_2	CuO	Al_2O_3	P_2O_5	Fe_2O_3	MnO_2	Identification	CuO/SiO_2
CAD-001-26.0a	46.59	37.66	1.54	n/d	n/d	n/d	Al-Chrys	0.81
CAD-001-26.0a	48.50	37.06	1.65	n/d	n/d	n/d	Al-Chrys	0.76
CAD-001-26.0a	46.02	37.14	1.38	n/d	n/d	n/d	Al-Chrys	0.81
CAD-001-26.0a	47.30	37.61	1.53	n/d	n/d	n/d	Al-Chrys	0.80
CAD-001-26.0a	47.25	37.82	1.54	n/d	n/d	n/d	Al-Chrys	0.80
CAD-001-26.0a	46.99	35.85	1.54	n/d	n/d	n/d	Al-Chrys	0.76
CAD-001-26.0a	32.48	22.77	1.01	n/d	n/d	n/d	Al-Chrys	0.70
CAD-001-26.0a	32.89	21.91	1.45	n/d	n/d	n/d	Al-Chrys	0.67

Sample	SiO_2	CuO	Al_2O_3	P_2O_5	Fe_2O_3	MnO_2	Identification	CuO/SiO_2
CAD-001-164.9	32.37	8.16	8.60	n/d	7.02	n/d	CuO+Phyllo	0.25
CAD-001-164.9	58.49	n/d	12.57	n/d	n/d	n/d	Felds	n/a

CAD-001-164.9	61.84	n/d	11.43	n/d	n/d	n/d	Felds	n/a
CAD-001-164.9	5.47	7.66	1.10	n/d	30.67	1.48	Goethite	n/a
CAD-001-164.9	5.18	7.29	n/d	n/d	33.47	n/d	Goethite	n/a
CAD-001-164.9	101.09	n/d	n/d	n/d	n/d	n/d	Qtz	n/a
CAD-001-164.9	63.28	n/d	10.67	n/d	n/d	n/d	Phyllo	n/a
CAD-001-164.9	43.98	n/d	15.08	n/d	2.29	n/d	Phyllo	n/a
CAD-001-164.9	46.66	n/d	15.81	n/d	1.51	n/d	Phyllo	n/a
CAD-001-164.9	4.71	6.41	2.21	n/d	32.06	1.37	Goethite	n/a
CAD-001-164.9	5.04	6.20	2.20	n/d	32.03	1.36	Goethite	n/a

Appendix 3

Interpretation of Electron Microprobe Analysis

Sample CARC-042 (Surface): Aluminum bearing Chrysocolla

This sample of fracture coating, pale blue-green to blue, chrysocolla was taken from outcrop at the CARC-042 drill pad. CuO varies from ~18% to 41%, but the CuO/SiO_2 ratio stays relatively constant, ranging from 0.70 to 0.88, suggesting that the level of hydration of the chrysocolla varies. Al_2O_3 ranges from ~1.1% to ~1.5%. The green color is likely the result of minor iron staining

Sample CAD-001-13.0: Unidentified iron and copper bearing silicate

This sample is an olive green fracture coating. CuO varies from ~6.5 % to ~11.0%. Total percentages of the six elements analyzed for do not add up to 100%, so some unidentified element or elements are unaccounted for. This material yielded copper in the field using the HCl/iron nail test.

Sample CAD-001-26.0: Aluminum bearing Chrysocolla

This sample is a sky blue fracture coating with bleached margins. In the bulk of the sample, CuO varies from ~28% to ~41%. In the bleached areas, CuO varies from ~15% to ~22%. The CuO/SiO_2 ratio stays relatively constant, ranging from 0.70 to 0.83, suggesting that the bleached chrysocolla is more hydrated then the sky blue chrysocolla. Al_2O_3 stays constant at ~1.3% to ~1.5%.

Sample CAD-001-50.4: Chrysocolla, Pseudo-malachite and "Neotocite"

This sample contains a physical mixture blue chrysocolla, sprays of green pseudo-malachite, and spots of black "neotocite". Chrysocolla contains ~51% CuO and unlike CAD-001-26.0, contains negligible Al_2O_3. The CuO/SiO_2 ratio is approximately 1.06. Pseudo-malachite is a hydrous copper phosphate which contains ~64% to ~66% CuO. "Neotocite" is a hydrous mineraloid of high variable composition. Various portions of this sample have a SiO_2 range from ~14% to ~30%, MnO_2 from ~8% to ~37% and Fe_2O_3 from <1% to ~8%. However, CuO stays relatively stable at ~30% to ~37%

Sample CAD-001-74.7: Chrysocolla

This sample is an encrustation of blue chrysocolla. CuO varies from ~47% to ~51%, the CuO/SiO_2 ratio is approximately 1.01 and Al_2O_3 content is negligible.

Sample CAD-001-85.4: Copper bearing Hematite and Goethite

This sample is a dark red to black fracture filling. SiO_2 ranges from ~2.5% to ~3.5%, MnO_2 from <1% to ~2.5%, and CuO from ~2% to ~2.5%. This sample yielded a little copper in the field using the HCl/iron nail test.

Sample CAD-001-164.9 : Copper bearing mixture of iron oxide and phyllosilicate (?)

This sample is a dark brown to black encrustation. CuO ranges from ~6% to ~8% and MnO_2 from <1% to ~1.5%. This sample yielded copper in the field using the HCl/iron nail test.

Appendix 4

Interpretation of XRD Results

Sample CAD-001-13.0 m: Berlinite ($AlPO_4$)

In hand specimen, this sample is a shiny dark brown coating on sky blue chrysocolla in a fracture. Although the major berlinite peaks are identifiable, the background noise level is high, which suggests that a pure sample was not obtained.

Sample CAD-001-26.0 m: Berlinite

This sample is a grainy dark brown coating on what is identified in hand specimen as sky blue chrysocolla filling a fracture. The major berlinite peak has high signal intensity.

Sample CAD-001-32.0 m: Kaolinite and Chrysocolla (?)

This sample is a sky blue fracture filling with traces of a shiny black material. XRD results show only three small peaks with no other signal above background noise. The small height of the kaolinite peaks suggests that kaolinite makes up only a small portion of this sample. Due to the amorphous nature of chrysocolla (which results in a weak to non-existent XRD signal) the lack of signal suggests that chrysocolla likely comprises much of this sample.

Sample CAD-001-52.5 m: Goethite and Hematite

In hand specimen, this sample is a spongy reddish brown material fracture filling. The greater intensity of the goethite peaks relative to that of the hematite peaks suggests that goethite predominates in the sample.

Sample CAD-001-71.1 m: Illite, Kaolinite, Goethite and Chlorite

Brownish black spots on a greenish brown fracture coating. This is typical of what was being described as "neotocite" spots in the core logs during the period of field sampling.

Sample CAD-001-85.4 m: Berlinite

Black coating on an epithermal quartz vein which crosscuts the porphyry. The vein is coarsely crystalline with box works that appear to be after oxidized sulfides.

Sample CAD-001-115.0 m: Quartz and Malachite

Massive brownish black and green filling of box work. The box work appears to be after oxidized sulfides. The greater intensity of the quartz signals suggests that there is more quartz than malachite in this sample.

Sample CAD-001-125.1 m: Malachite

A grainy, light green, fracture coating. The very intense malachite peaks suggest that this sample is quite pure.

Sample CAD-001-138.5 m: Malachite

Sprays of small (~ 1 mm) green crystals on a brownish black fracture coating. Care was taken during analysis to sample only green crystals and to avoid substrate. Malachite peaks are strong and abundant, suggesting a pure sample.

Sample CAD-001-164.9 m: Berlinite and Quartz

A shiny black encrustation on a fracture. Intensity of the quartz peaks is minor compared to that of the berlinite peaks, so it is likely that berlinite is the major phase in the sample.

Sample CAD-001-172.8 m: Kaolinite, Berlinite and Hematite

An earthy, light brown, fracture coating. All minerals display clear, distinct peaks. Kaolinite has the highest intensity peaks while berlinite and hematite have peaks approximately one third as intense as kaolinite.

Sample CAD-002-41.5 m: Chrysocolla (?), Kaolinite, Quartz and Chlorite

A sky blue and lavender fracture filling, with thin brown coating between chrysocolla and wallrock. The kaolinite and quartz peaks are very small and no other signal is present, which implies much of the sample is not producing a XRD signal. The lavender color of what appears to be chysocolla may be due either to kaolinite or to very minor staining by brown substrate.

Sample CAD-002-60.2 m: Malachite, Quartz and Illite

A dark blue-green encrustation on a reddish brown fracture coating. Illite is minor.

Appendix 5

Fluid Inclusions

Doubly polished wafers were used in all fluid inclusion analyses and were performed on a Linkam heating stage using 40 and 80 power objectives.

P = Primary, S = Secondary

Th = Homogenization Temperature, Tm = Final Melting Temperature

CAD 002 46.9

Number	Size (mm)	Type	Phases	Fill	Th (°C)	Tm (°C)	Salinity eq.wt.%NaCl
1	7	p	2(L+V)	0.85	346.1	-4.2	6.7
2	2	p	2(L+V)	0.90	331.8	-3.6	5.8
3	3	p	2(L+V)	0.95	350.3	-6.0	9.2
4	7	p	2(L+V)	0.90	345.7	-2.6	4.2
5	4	p	2(L+V)	0.85	380.2	-4.2	6.7
6	9	p	2(L+V)	0.90	356.8	-7.0	10.5
7	2	p	2(L+V)	0.90	369.8	-6.2	9.5
	Duplicate					-6.3	
8	4	p	2(L+V)	0.95	374.5	-7.2	10.7
9	8	p	2(L+V)	0.90	335.7	-5.5	8.5
10	6	p	2(L+V)	0.90	360.1	-4.8	7.5
11	5	s	2(L+V)	0.95	211.5	-2.5	4.1
12	13	s	2(L+V)	0.85	223.8	-6.5	9.8
13	2	s	2(L+V)	0.85	244.4	-3.9	6.2
	Duplicate				245.2		
14	4	s	2(L+V)	0.80	240.8		

15	5	s	2(L+V)	0.95	229.6		
16	6	s	2(L+V)	0.90	211.8		
17	4	s	2(L+V)	0.85	240.1		

CAD 002 86.5

Number	Size (mm)	Type	Phases	Fill	Th (°C)	Tm (°C)	Salinity eq.wt.%NaCl
1	7	p	2(L+V)	0.80	365.3	-7.1	10.6
2	14	p	2(L+V)	0.80	376.7	-3.9	6.2
3	13	p	2(L+V)	0.90	364.3	-3.0	4.9
4	8	p	2(L+V)	0.95	375.4	-3.4	5.5
	Duplicate				373.9		
5	5	p	2(L+V)	0.80	383.8	-6.8	10.2
6	6	p	2(L+V)	0.85	356.2	-5.9	9.1
7	9	p	2(L+V)	0.95	379.8	-5.4	8.4
8	8	p	2(L+V)	0.90	343.2	-8.9	12.7
9	3	p	2(L+V)	0.85	347.5	-9.2	13.1
	Duplicate					-9.1	
10	15	p	2(L+V)	0.95	355.2	-6.5	9.8
11	7	p	2(L+V)	0.90	361.3		
12	4	p	2(L+V)	0.90	330.1		
13	10	p	2(L+V)	0.95	385.9		
14	11	p	2(L+V)	0.90	366.2		
15	8	p	2(L+V)	0.85	392.7		
16	4	p	2(L+V)	0.80	347.6		
17	7	p	2(L+V)	0.95	342.7		

18	2	s	2(L+V)	0.80	250.1	-6.2	9.5
19	3	s	2(L+V)	0.80	259.3	-5.1	8.0
CAD 002 87.5							
Number	Size	Type	Phases	Fill	Th	Tm	Salinity
	(mm)				(°C)	(°C)	eq.wt.%NaCl
1	4	p	2(L+V)	0.85	384.5	-2.7	4.4
2	6	p	2(L+V)	0.90	345.6	-5.7	8.8
3	12	p	2(L+V)	0.90	344.8	-4.7	7.4
4	6	p	2(L+V)	0.90	389.1	-4.3	6.8
5	3	p	2(L+V)	0.85	389.0	-3.2	5.2
	Duplicate				391.1		
6	5	p	2(L+V)	0.90	391.5	-4.3	6.8
7	3	p	2(L+V)	0.95	342.6	-3.3	5.3
8	5	p	2(L+V)	0.90	335.9	-3.4	5.5
9	8	p	2(L+V)	0.99	360.8	-4.9	7.7
10	8	p	2(L+V)	0.90	357.5	-6.2	9.5
11	7	p	2(L+V)	0.95	351.1	-6.6	10.0
12	2	p	2(L+V)	0.95	343.5	-4.5	7.1
13	6	p	2(L+V)	0.90	382.8	-4.9	7.7
14	4	p	2(L+V)	0.85	387.9		
15	4	p	2(L+V)	0.85	340.2		
16	3	s	2(L+V)	0.80	242.7	-2.9	4.7
17	6	s	2(L+V)	0.85	258.9	-2.9	4.7
	Duplicate					-3.0	
18	2	s	2(L+V)	0.90	260.0	-1.9	3.1
19	3	s	2(L+V)	0.80	242.5	-3.2	5.2

20	3	s	2(L+V)	0.85	238.2	-3.9	6.2
21	5	s	2(L+V)	0.80	219.2	-4.7	7.4

CAD 001 108

Number	Size (mm)	Type	Phases	Fill	Th (°C)	Tm (°C)	Salinity eq.wt.%NaCl
1	3	p	2(L+V)	0.95	386.5		
2	5	p	2(L+V)	0.90	363.4		
3	6	p	2(L+V)	0.95	362.5		
	Duplicate				365.0		
4	4	p	2(L+V)	0.95	345.4		
5	4	p	2(L+V)	0.90	349.7		
6	6	p	2(L+V)	0.90	334.4		
7	8	s2	2(L+V)	0.85	292.5	-7.1	10.6
	Duplicate					-7.0	
8	5	s	2(L+V)	0.85	309.6	-4.2	6.7
9	4	s	2(L+V)	0.80	303.9	-3.6	5.8
10	6	s	2(L+V)	0.85	303.1		
11	2	s	2(L+V)	0.90	286.5		
12	4	s	2(L+V)	0.80	315.7		
13	5	s	2(L+V)	0.85	283.2		
14	5	s	2(L+V)	0.80	318.4		
15	3	s	2(L+V)	0.90	303.1		
16	2	s	2(L+V)	0.80	214.4	-6.5	9.8
17	3	s	2(L+V)	0.80	190.8	-5.5	8.5
18	3	s	2(L+V)	0.85	251.2		

CAD 002 123

Number	Size (mm)	Type	Phases	Fill	Th (°C)	Tm (°C)	Salinity eq.wt.%NaCl
1	2	p	2(L+V)	0.90	371.1	-2.2	3.6
2	4	p	2(L+V)	0.90	351.6	-3.2	5.2
3	4	p	2(L+V)	0.85	380.6	-7.5	11.1
4	7	p	2(L+V)	0.90	397.3	-4.0	6.4
5	4	p	2(L+V)	0.95	388.8	-4.9	7.7
6	5	p	2(L+V)	0.90	364.3	-5.7	8.8
7	5	p	2(L+V)	0.85	394.5	-3.2	5.2
8	4	p	2(L+V)	0.90	347.2	-6.8	10.2
9	3	p	2(L+V)	0.85	336.7	-3.2	5.2
10	7	p	2(L+V)	0.90	340.1	-4.7	7.4
11	6	p	2(L+V)	0.90	390.5		
12	4	p	2(L+V)	0.85	364.9		
13	9	p	2(L+V)	0.90	322.8		
14	11	p	2(L+V)	0.90	323.1		
	Duplicate				320.5		
15	6	s	2(L+V)	0.80	225.9	-2.5	4.1
16	3	s	2(L+V)	0.85	232.8	-3.1	5.0
	Duplicate					-3.0	
17	5	s	2(L+V)	0.90	246.2	-4.0	6.4

18	4	s	2(L+V)	0.80	219.9	-2.8	4.5
19	2	s	2(L+V)	0.85	213.5		
20	3	s	2(L+V)	0.80	225.7		

CAD 002 194.5

Number	Size (mm)	Type	Phases	Fill	Th (°C)	Tm (°C)	Salinity eq.wt.%NaCl
1	3	p	2(L+V)	0.90	379.5	-7.9	11.6
	Duplicate					-8.0	
2	6	p	2(L+V)	0.90	346.9	-5.0	7.8
3	7	p	2(L+V)	0.95	372.7	-4.8	7.5
4	4	p	2(L+V)	0.95	380.6	-4.0	6.4
	Duplicate				377.7		
5	4	p	2(L+V)	0.85	365.2	-5.3	8.2
6	4	p	2(L+V)	0.85	370.0		
7	8	p	2(L+V)	0.80	380.2		
8	7	p	2(L+V)	0.90	338.1		
9	4	p	2(L+V)	0.90	348.3		
10	6	s	2(L+V)	0.85	251.6	-5.2	8.1
11	2	s	2(L+V)	0.90	244.2	-7.9	11.6
12	3	s	2(L+V)	0.90	259.8	-5.3	8.2
13	4	s	2(L+V)	0.80	243.2	-4.3	6.8
14	4	s	2(L+V)	0.85	235.6	-7.1	10.6
15	5	s	2(L+V)	0.90	240.0	-6.4	9.7
16	4	s	2(L+V)	0.80	250.1		

17	3	s	2(L+V)	0.85	230.3		
18	4	s	2(L+V)	0.80	227.5		
19	3	s	2(L+V)	0.80	230.1		
20	2	s	2(L+V)	0.80	251.3		

CAD 003 263

Number	Size (mm)	Type	Phases	Fill	Th (°C)	Tm (°C)	Salinity eq.wt.%NaCl
1	9	p	2(L+V)	0.85	330.6	-4.8	7.5
2	5	p	2(L+V)	0.95	331.2	-2.9	4.7
	Duplicate					-2.8	
3	11	p	2(L+V)	0.90	381.4	-4.7	7.4
4	5	p	2(L+V)	0.90	335.2	-5.2	8.1
5	3	p	2(L+V)	0.95	336.5	-5.1	8.0
6	10	p	2(L+V)	0.95	341.3	-5.9	9.1
7	7	p	2(L+V)	0.85	381.7	-3.7	5.9
8	8	p	2(L+V)	0.90	336.5	-5.6	8.7
9	6	p	2(L+V)	0.90	350.8	-3.2	5.2
10	4	p	2(L+V)	0.95	358.4		
11	5	p	2(L+V)	0.95	361.9		
12	7	p	2(L+V)	0.85	388.8		
13	7	p	2(L+V)	0.90	330.1		
14	5	p	2(L+V)	0.80	386.1		
15	4	s	2(L+V)	0.80	190.8	-3.7	5.9
	Duplicate				192.3		

16	3	s	2(L+V)	0.85	210.5	-4.2	6.7
17	2	s	2(L+V)	0.85	254.7	-6.0	9.2

0201892-8117092; Rosa Maria vein

Number	Size (mm)	Type	Phases	Fill	Th (°C)	Tm (°C)	Salinity eq.wt.%NaCl
1	~1	p	2(L+V)	0.95	260-275		
2	~1	p	2(L+V)	0.95	260-275		
3	~1	p	2(L+V)	0.95	250-280		
4	~1	p	2(L+V)	0.95	250-280		
5	~1	p	2(L+V)	0.95	260-280		
6	~1	p	2(L+V)	0.95	260-280		
7	~1	p	2(L+V)	0.95	250-270		

Appendix 6

Fluid Inclusion Duplicate Measurments

Th_i = Initial Homogenization Temperature, Th_d = Duplicate

Tm_i = Initial Melting Temperature, Tm_d = Duplicate

Homogenization Tempeature

Sample	Th_i	Th_d
	(^oC)	
CAD 002 46.9	244.4	245.2
CAD 002 86.5	375.4	373.9
CAD 002 87.5	389.0	391.1
CAD 001 108	362.5	365.0
CAD 002 123	323.1	320.5
CAD 002 194.5	380.6	377.7
CAD 003 262	190.8	192.3

Melting Temperatuere

Sample	Tm_i	Tm_d
	eq. wt .% NaCl	
CAD 002 46.9	-6.2	-6.3
CAD 002 86.5	-9.2	-9.1
CAD 002 87.5	-2.9	-3.0
CAD 001 108	-7.1	-7.0
CAD 002 123	-3.1	-3.0
CAD 002 194.5	-7.9	-8.0
CAD 003 262	-2.9	-2.8

Appendix 7

Oxygen Isotope Analysis of National Bureau of Standards NBS-28

Reported value of NBS-28 is $d^{18}O = 9.64\ ^{o}/_{oo}$ vs. VSMOW

Date	Vessel	$d^{18}O$ ($^{o}/_{oo}$)	yield (%)	average ($^{o}/_{oo}$)	range
6/5/00	1	9.182	108.3	9.100	+/- 0.242
6/5/00	3	9.057	104.0		
6/5/00	4	9.180	108.3		
6/5/00	5	9.154	103.4		
6/5/00	6	9.264	106.5		
6/5/00	7	9.084	107.8		
6/5/00	8	9.181	106.2		
6/5/00	9	9.259	109.5		
6/5/00	10	9.056	107.8		
6/5/00	11	9.194	103.0		
6/5/00	12	9.155	105.6		
6/10/00	2	9.010	110.1		
6/10/00	5	8.965	109.9		
6/10/00	6	8.957	107.6		
6/10/00	7	8.885	110.3		
6/10/00	8	9.092	108.4		
6/10/00	9	9.151	110.7		
6/10/00	10	8.899	113.6		
6/10/00	11	8.938	110.3		
6/10/00	12	8.972	104.1		
6/13/00	4	9.310	110.2		
6/13/00	9	9.369	109.3		
6/18/00	11	9.117	110.4		
6/18/00	12	9.201	109.3		
6/20/00	1	8.880	111.8		
6/20/00	10	8.964	113.2		
6/24/00	1	9.067	107.9		
6/24/00	10	9.246	106.7		

Appendix 8
Oxygen Isotope Analysis

Yield was estimated for whole rock samples by calculating the amount of oxygen produced from an equal amout of quartz.
* indicates a duplicate sample.

Date	Vessel	Sample	Sample Type	Weight (mg)	$d^{18}O$ ‰	Std. Dev.	Yield %
6/13/00	2	West Yanomayo	quartz	10.7	14.916	0.041	110.2
6/13/00	5	Lourdes	quartz	10.6	13.947	0.047	101.2
6/13/00	6	Yanomayo	quartz	10.4	13.091	0.071	110.1
6/13/00	7	Rosa Maria	quartz	10.7	11.272	0.064	104.4
6/13/00	8	Lourdes	quartz	10.6	13.707	0.063	109.8
6/13/00	10	Cahuintala	quartz	10.5	10.203	0.039	104.0
6/13/00	11	Saturno	quartz	10.7	11.038	0.071	109.9
6/13/00	12	Saturno*	quartz	10.5	11.308	0.045	106.5
6/18/00	2	Saturno*	quartz	10.600	10.825	0.086	113.6
6/18/00	4	Rosa Maria*	quartz	10.700	10.628	0.080	108.2
6/18/00	5	Rosa Maria*	quartz	10.700	10.240	0.030	111.0
6/18/00	6	Cahuintala*	quartz	10.500	9.964	0.048	102.1
6/18/00	7	Cahuintala*	quartz	10.400	10.383	0.048	106.3
6/18/00	8	Yanomayo*	quartz	10.400	13.005	0.093	103.1
6/18/00	9	Lourdes*	quartz	10.800	13.631	0.044	103.8
6/18/00	10	West Yanomayo*	quartz	10.300	15.285	0.024	106.8

6/20/00	3	CAD-003-127	quartz	10.2	9.036	0.074	111.1
6/20/00	4	CAD-002-87.5	quartz	10.3	8.978	0.085	108.3
6/20/00	5	CAD-002-213.4	quartz	10.5	8.781	0.024	106.6
6/20/00	6	CAD-002-213.4*	quartz	10.7	8.931	0.064	108.0
6/20/00	7	CAD-001-104	quartz	10.4	11.771	0.073	105.0
6/20/00	8	CAD-002-86.5	quartz	10.1	9.027	0.077	111.7
6/20/00	9	CAD-002-213.4	whole rock	10.1	8.414	0.047	99.3
6/20/00	11	CAD-001-110.6	whole rock	10.6	8.879	0.088	104.0
6/20/00	12	CAD-001-110.6*	whole rock	10.7	8.973	0.083	102.7
6/23/00	3	CAD-001-108	quartz	10.5	8.420	0.064	110.9
6/23/00	5	CAD-001-97.4	quartz	10.3	9.358	0.019	110.7
6/23/00	6	CAD-001-97.4*	quartz	10.6	9.284	0.057	113.9
6/23/00	8	CAD-001-140.5	whole rock	10.4	8.338	0.086	101.1
6/23/00	9	CAD-001-140.5*	whole rock	10.2	8.728	0.095	101.8
6/23/00	10	CAD-001-102.4	whole rock	10.4	6.773	0.093	105.5
6/23/00	11	CAD-002-14.2	whole rock	10.2	8.746	0.097	99.9
6/24/00	3	CAD-003-263	quartz	10.7	8.779	0.046	108.0
6/24/00	4	CAD-002-194.5	quartz	10.1	9.177	0.060	106.0
6/24/00	5	CAD-002-46.9	quartz	10.0	9.152	0.098	106.0
6/24/00	6	CAD-001-129.2	quartz	10.4	9.184	0.065	110.0
6/24/00	7	CAD-003-48.9	whole rock	10.4	9.291	0.063	99.6
6/24/00	8	CAD-002-26.8	whole rock	10.2	9.260	0.053	100.9
6/24/00	9	CAD-002-26.8*	whole rock	10.1	9.218	0.072	99.0
6/24/00	11	0203370-8118795	whole rock	10.5	11.359	0.065	98.2
6/24/00	12	0204685-8118299	whole rock	10.7	9.345	0.091	93.3

7/13/00	7	CAD-001-102.4*	whole rock	10.0	6.918	0.070	98.3
7/13/00	9	0203481-8118741	whole rock	10.8	10.702	0.048	103.5

This Thesis is accepted on behalf of the faculty
of the Institute by the following committee:

Andrew Campbell

Academic Adviser

William K. Chiu

Research Advisor

David L. Norman

Committee Member

Committee Member

Committee Member

Feb 2 2001

Date